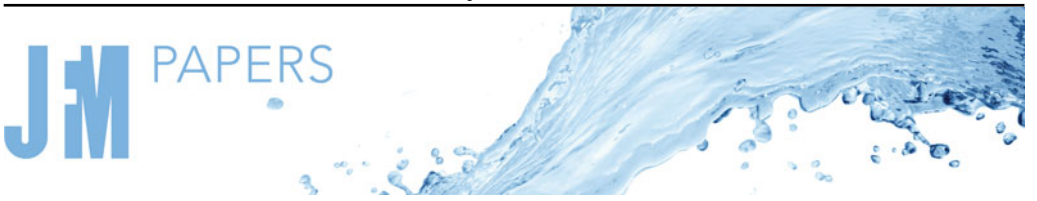
J. Fluid Mech. (2026), *vol.* 1039, A26, doi:10.1017/jfm.2026.11809



Low-frequency bandgaps for water waves enabled by flexible plate metamaterials

Huaqing Jin[1,2], **Haicheng Zhang**[1], **Siming Zheng**[3,4], **Xiaofan Li**[2], **Ye Lu**[5,6], **Daolin Xu**[7] **and Deborah Greaves**[4,8]

[1]College of Mechanical and Vehicle Engineering, Hunan University, Changsha 410082, PR China

[2]Department of Mechanical Engineering, The University of Hong Kong, Hong Kong 999077, PR China

[3]Ocean College, Zhejiang University, Zhoushan 316021, PR China

[4]School of Engineering, Computing and Mathematics, University of Plymouth, Drake Circus, Plymouth PL4 8AA, UK

[5]China Ship Scientific Research Center, Wuxi, 214082, PR China

[6]Taihu Laboratory of Deep Sea Science, Wuxi 214082, PR China

[7]Fuyao University of Science and Technology, Fuzhou 350100, PR China

[8]Department of Engineering Science, University of Oxford, Parks Road, Oxford, OX1 3PJ, UK

Corresponding authors: Haicheng Zhang, zhanghc@hnu.edu.cn; Siming Zheng, siming.zheng@plymouth.ac.uk

(Received 26 March 2026 UTC; revised 19 May 2026 UTC; accepted 12 June 2026 UTC)

This study investigates a novel class of flexible plate metamaterials (FPMMs), consisting of a periodic array of bottom-mounted flexible structures, designed for the sub-wavelength manipulation of surface gravity waves. A theoretical framework is developed by coupling the matched eigenfunction expansion method with a modal expansion technique, incorporating Bloch's theorem to characterise the band structures and complex dispersion relations. Numerical analysis reveals that the structural flexibility facilitates the formation of low-frequency, broadband bandgaps, primarily driven by a local resonance (LR) mechanism. It is shown that wave propagation can be effectively suppressed within these bandgap regimes through the synergistic interaction between the incident wave field and the structural vibration modes. The theoretical predictions are validated through laboratory experiments conducted in a wave flume, where substantial wave attenuation was observed under resonant conditions. Notably, the LR-induced bandgaps occur at significantly lower frequencies and exhibit broader bandwidths compared to those arising from traditional Bragg resonance. These findings demonstrate that the proposed FPMMs provide a tunable and effective mechanism for sub-wavelength wave attenuation, offering fundamental insights into localised hydrodynamic wave control.

Key words: wave-structure interactions, wave scattering, surface gravity waves

© The Author(s), 2026. Published by Cambridge University Press.

https://doi.org/10.1017/jfm.2026.11809 Published online by Cambridge University Press

1. Introduction

Ocean waves pose significant threats to coastal regions, driving severe erosion and inflicting potential damage on marine infrastructure (Dai *et al.* 2018). Consequently, the development of effective strategies to protect coastal and offshore structures from wave-induced impacts is of critical importance (Jin *et al.* 2022).

In recent years, the development of metamaterials/metastructures has provided a revolutionary approach for wave control. These artificial structures, typically arranged in periodic patterns at a sub-wavelength scale, exhibit properties not found in nature (Liu & Zhang 2011; Zheludev & Kivshar 2012). The study of metamaterials has thrived in fields such as electromagnetism, optics, acoustics and elastic waves (Sihvola 2007; Ma & Sheng 2016; Lee & Kim 2023). As a wave phenomenon, surface gravity waves share many similarities with other classical waves, such as electromagnetic waves and acoustic waves. Therefore, the theories and methods used to manipulate these waves can inform research on surface gravity waves (Mei *et al.* 2018; Liang *et al.* 2024). Torres *et al.* (1999) visualised Bloch waves of surface gravity waves over a periodically drilled bottom, demonstrating that surface gravity waves possess the band structure akin to electromagnetic/acoustic waves, indicating that the metamaterial method may be used to engineer water wave propagation. Some studies have explored these ideas in different systems. Hu & Chan (2005) realised refraction propagation of water waves with an array of bottom-mounted vertical cylinders, which can be viewed as metamaterials, thereby providing a mechanism to control the flow of ocean wave energy. Berraquero *et al.* (2013) conducted quantitative experimental examination of water wave manipulation employing a metamaterial composed of layered structured bathymetry. Their findings showcased that anisotropic metamaterial can be used in the realm of water waves to create a reflectionless bent waveguide. Motivated by the concept of electromagnetic waveguide cloaks employing gradient index metamaterials, Zou *et al.* (2019) employed the mode conversion mechanism, and fabricated a broadband waveguide cloak for water waves with a simple gradient depth bar on the water bottom. Zheng *et al.* (2020, 2024) and Porter *et al.* (2022) conducted research on a metamaterial cylinder formed by a closely spaced thin plate. Their theoretical results showed that wave focusing, blocking, negatively refracted transmission and wide-band energy capture could be achieved using different metamaterial configurations. Zhu *et al.* (2024) reported developments in the control of water waves with metamaterials, summarising the basic theory and calculation approaches relevant to this emerging field. Those works collectively highlight the significant potential of metamaterials in manipulating water wave propagation.

As a key feature of metamaterials, the bandgap effect refers to a unique physical phenomenon in which waves are unable to propagate within a specific frequency range due to the synergistic interaction of periodic unit cells. This effect provides inspiration for achieving strong water wave attenuation. Analogous to studies in photonic and phononic crystals, the bandgap in periodic structures for water waves can be achieved through the Bragg resonance (BR) mechanism (Heathershaw 1982). However, BR requires the lattice period of the crystal to be a multiple of half the wavelength, making it challenging to attenuate long water waves using small-scale structures. The discovery of the local resonance (LR) mechanism paves the way for generating a low-frequency bandgap with the small-scaled metamaterial (Liu *et al.* 2000). Nevertheless, the LR metamaterials have been relatively underexploited in the realm of water waves, albeit with a few notable exceptions. Hu *et al.* (2011) designed a periodic array of vertical bottom-standing split tubes, in which the water column in the tube acted as a resonator. When waves encountered the tubes at the resonant frequency of the water column, negative effective gravity occurred and a low-frequency bandgap was found. In a parallel investigation, Dupont *et al.* (2017)

https://doi.org/10.1017/jfm.2026.11809 Published online by Cambridge University Press

carried out numerical simulations on water waves propagating through a periodic C-shaped vertical cylinder array, and found that there was a low-frequency bandgap below the BR bandgap, confirming that the low-frequency bandgap was induced by the water resonance in the C-shaped cylinders. Huang & Porter (2023) studied the water wave propagation through arrays of closely spaced vertical plates, and found that there exists a critical frequency that determines whether the wave can propagate through the array; the critical frequency relates to the water resonance in narrow channels. For the water wave LR metamaterials mentioned above, the liquid in the channel functions as a local resonator, and the incident wave can be slowed down due to a progressive transfer of energy between the waveguide and the resonators. In addition to the oscillating water resonators, the oscillating body (OB) resonators appear to possess similar properties. De Vita *et al.* (2021) introduced mechanical metamaterials designed to attenuate surface gravity waves. The mechanical metamaterials are made of four OB resonators immersed in a fluid and forced by water waves. Their study found that these OB resonators could dissipate wave energy effectively, and the peak wave attenuation occurs when the frequency of the wave and the frequency of the resonators approximately coincide. Later, Lorenzo *et al.* (2023) carried out an experimental study on wave attenuation using an array of submerged cylindrical pendulums. Their tests explored various system parameters, demonstrating significant wave attenuation when the incident wave frequency approached the natural frequency of the pendulums. More recently, through the integration of power take-off devices, OB resonators can function as wave energy converters, enabling nearly perfect absorption of water wave energy (Westcott *et al.* 2024). Furthermore, by incorporating a gradient in the resonant frequencies of the resonators, the so-called rainbow trapping effect can be realised, leading to the formation of a broadband bandgap (Liu *et al.* 2025).

Despite these advancements, the application of LR metamaterials for controlling surface gravity waves – the dominant wave type in oceanic and coastal environments – remains relatively underexplored. The central frequency of an LR bandgap is fundamentally governed by the intrinsic resonance characteristics of the constituent resonators (Sheng *et al.* 2003). Achieving sub-wavelength bandgaps that are compatible with marine environments therefore requires flexible and efficient strategies for tuning the resonant frequency of the oscillators (Jin *et al.* 2024). In the present work, we introduce a novel class of OB metamaterials employing submerged flexible plates as the primary resonant elements. Arranged periodically on the seabed, these bio-inspired structures exploit hydroelastic deformation – reminiscent of submerged aquatic vegetation – to interact dynamically with the incident wave field (Nové-Josserand *et al.* 2019; Zhu *et al.* 2020). In contrast to conventional rigid resonators, the intrinsic flexibility of the plates provides an additional tunable degree of freedom, enabling the resonant modes and associated bandgaps to be shifted towards lower frequencies through stiffness modulation, rather than solely through increasing the physical size of the system. However, the transition from discrete rigid resonators to flexible continua introduces significant theoretical complexities, as the hydroelastic response involves an infinite spectrum of vibration modes, each coupled with both propagating and evanescent wave components. Analytically capturing these interactions within a periodic framework requires a rigorous treatment of the boundary-value problem to resolve the complex dispersion relations and the emergent band structure.

The remainder of this paper is organised as follows. In § 2, we formulate a rigorous theoretical model for the interaction between surface gravity waves and flexible plate metamaterials (FPMMs) within the framework of potential flow theory. The coupled scattering and radiation problem for finite-size FPMMs is solved via the matched eigenfunction expansion method integrated with a modal expansion technique, while the

https://doi.org/10.1017/jfm.2026.11809 Published online by Cambridge University Press

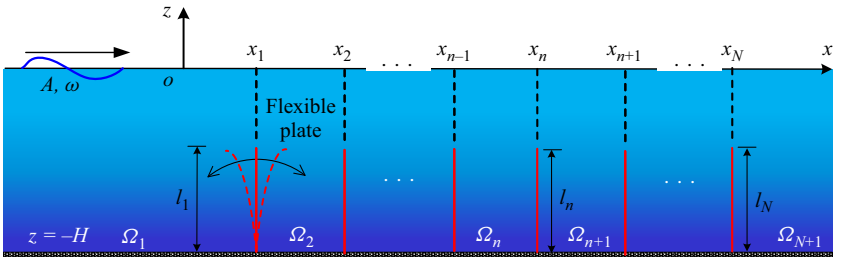


Figure 1. Schematic of an array of flexible plates, oscillating under excitation of the incident wave, forming the so-called metamaterials.

band structures for infinite arrays are derived through the application of Bloch's theorem. Section 3 presents a detailed numerical investigation into the LR mechanisms, specifically examining how structural flexibility modulates wave inhibition and bandgap topology. In § 4, the theoretical predictions are benchmarked against laboratory experiments conducted in a precision wave flume, emphasising the observation of broadband attenuation under sub-wavelength conditions. Finally, concluding remarks and prospects for future research are provided in § 5.

2. Problem formulation

2.1. *Governing equations and general solutions*

Referring to figure 1, we consider an array of bottom-standing flexible plates embedded in a fluid domain Ω of infinite horizontal extent and finite depth H. A two-dimensional Cartesian coordinate system (x, z) is introduced, with the x-axis oriented horizontally, and the z-axis measured vertically upwards. The flat seabed and undisturbed free surface are located at $z = -H$ and $z = 0$, respectively. The array consists of N flexible plates, with the nth plate positioned at $x = x_n$ and extending over the vertical interval $-H \le z \le -d_n$, where $x_n \in \mathbb{R}$ for $n \in \{1, 2, \ldots, N\}$, and $l_n = H - d_n$ denotes the plate length, with d_n representing the submergence depth of the plate's upper edge. From a design perspective, the spacing between adjacent plates $(x_{n+1} - x_n)$ must be larger than the sum of their maximum horizontal tip excursions to prevent physical collisions, particularly under resonant conditions where the hydroelastic response is maximised.

As in many gravity wave problems (Falnes 2002), the fluid is assumed to be inviscid and incompressible, and the motion is taken to be irrotational. Linear wave theory is therefore adopted throughout this work. The velocity field admits a potential representation $\Phi(x, z, t) = \mathrm{Re}[\phi(x, z)\, \mathrm{e}^{-\mathrm{i}\omega t}]$, where Re denotes the real part, ϕ is the complex-valued spatial velocity potential, ω is the angular frequency, and $\mathrm{i} = \sqrt{-1}$ is the imaginary unit. In the same spirit, the motion of each flexible plate is assumed to be harmonic and linear, so that the transverse deflection of the nth plate can be written as $W_n(z, t) = \mathrm{Re}[w_n(z)\, \mathrm{e}^{-\mathrm{i}\omega t}]$.

2.1.1. *Flexible plate*

We begin with the structural dynamics of the flexible plates. The plates are taken to be slender and free of shear deformation, and are thus modelled as Euler–Bernoulli beams in the present two-dimensional setting. The linearised equation of motion of the nth plate reads

$$E_n I_n\, \partial_z^4 w_n - \omega^2 \rho_n b_n w_n = \mathrm{i}\omega\rho_w \left(\phi|_{x=x_n^-} - \phi|_{x=x_n^+}\right), \tag{2.1}$$

https://doi.org/10.1017/jfm.2026.11809 Published online by Cambridge University Press

where E_n is the Young's modulus of the plate, b_n is its thickness, $I_n = b_n^3/12$ is the second moment of area, ρ_n is the plate density, and ρ_w is the water density. Here, x_n^- and x_n^+ denote the fluid point immediately to the left and right of the plate, respectively. The left-hand side of (2.1) represents the intrinsic structural response, arising from bending stiffness and inertia, whereas the right-hand side accounts for the hydrodynamic forcing induced by the pressure jump across the plate.

To solve for the structural deformation, the mode expansion method is employed, and the plate displacement is expanded as

$$w_n(z) = \sum_{m=1}^{\infty} \sigma_{n,m}\, w_{n,m}(z), \tag{2.2}$$

where $w_{n,m}(z)$ is the mth natural mode of the nth plate, and $\sigma_{n,m}$ is the corresponding complex modal amplitude. Each mode shape satisfies

$$\partial_z^4 w_{n,m} - (\kappa_{n,m})^4\, w_{n,m}(z) = 0, \tag{2.3}$$

with $(\kappa_{n,m})^4 = (\omega_{n,m})^2 \rho_n b_n/(E_n I_n)$, and $\omega_{n,m}$ denoting the associated eigenfrequency.

The clamped lower edge at the seabed and the free upper edge of the plate impose the boundary conditions

$$w_{n,m}\big|_{z=-H} = \partial_z w_{n,m}\big|_{z=-H} = 0, \tag{2.4a}$$

$$\partial_z^2 w_{n,m}\big|_{z=-d_n} = \partial_z^3 w_{n,m}\big|_{z=-d_n} = 0. \tag{2.4b}$$

The governing equation (2.3), together with the boundary conditions (2.4), yields the mode shape

$$\begin{aligned} w_{n,m}(z) = {} & \cos\big[\kappa_{n,m}(z+H)\big] - \cosh\big[\kappa_{n,m}(z+H)\big] \\ & - \xi_{n,m}\left\{\sin\big[\kappa_{n,m}(z+H)\big] - \sinh\big[\kappa_{n,m}(z+H)\big]\right\}, \end{aligned} \tag{2.5}$$

where

$$\xi_{n,m} = \frac{\cos\big(\kappa_{n,m} l_n\big) + \cosh\big(\kappa_{n,m} l_n\big)}{\sin\big(\kappa_{n,m} l_n\big) + \sinh\big(\kappa_{n,m} l_n\big)}, \tag{2.6}$$

and $\kappa_{n,m}$ is determined by

$$\cos\big(\kappa_{n,m} l_n\big)\cosh\big(\kappa_{n,m} l_n\big) + 1 = 0. \tag{2.7}$$

Having established the modal basis, we project the governing equation onto each mode. Multiplying (2.1) by $w_{n,\zeta}(z)$ and integrating over $[-H, -d_n]$, and then invoking the orthogonality of the natural modes, gives

$$\sigma_{n,\zeta}\big(E_n I_n \kappa_{n,\zeta}^4 - \omega^2 \rho_n b_n\big) l_n = F_{n,\zeta}, \tag{2.8}$$

where

$$F_{n,\zeta} = -\mathrm{i}\omega\rho_w \int_{-H}^{-d_n} \Delta\phi_n(z)\, w_{n,\zeta}(z)\, \mathrm{d}z \tag{2.9}$$

represents the hydrodynamic force acting on plate n in mode ζ, and

$$\Delta\phi_n(z) = \phi(x_n^+, z) - \phi(x_n^-, z) \tag{2.10}$$

denotes the potential jump across the plate.

https://doi.org/10.1017/jfm.2026.11809 Published online by Cambridge University Press

The principal mass and principal stiffness of the flexible plate are defined as

$$M_{n,m} = \int_{-H}^{-d_n} \rho_n b_n \left[w_{n,m}(z)\right]^2 \, \mathrm{d}z = l_n \rho_n b_n, \tag{2.11a}$$

$$K_{n,m} = \int_{-H}^{-d_n} E_n I_n \left[w''_{n,m}(z)\right]^2 \, \mathrm{d}z = \kappa_{n,m}^4 l_n E_n I_n. \tag{2.11b}$$

Accordingly, (2.1) can be recast in the compact form

$$\sigma_{n,\zeta}\left(K_{n,\zeta} - \omega^2 M_{n,\zeta}\right) = F_{n,\zeta}. \tag{2.12}$$

2.1.2. *Fluid problem*

We now turn to the fluid problem. The water motion is described by linear potential flow theory, such that the velocity field is given by the gradient of the scalar potential ϕ, which satisfies Laplace's equation in the fluid domain:

$$\nabla^2 \phi = 0 \quad \text{for all } (x, z) \in \Omega. \tag{2.13}$$

At the free surface, the linearised dynamic and kinematic conditions yield

$$\partial_z \phi = \frac{\omega^2}{g}\phi \quad \text{at} \quad z = 0, \tag{2.14}$$

while the impermeable seabed imposes

$$\partial_z \phi = 0 \quad \text{on} \quad z = -H. \tag{2.15}$$

On the wetted surface of plate n, the kinematic condition enforces continuity of normal velocity:

$$\partial_x \phi = -\mathrm{i}\omega w_n(z) \quad \text{for} \quad (x, z) \in \Gamma_n^p, \tag{2.16}$$

where $\Gamma_n^p = \{(x_n, z) \mid -H < z < -d_n\}$ denotes the submerged portion of plate n.

Substituting the modal expansion of w_n yields

$$\partial_x \phi = -\mathrm{i}\omega \sum_{m=1}^{\infty} \sigma_{n,m} \, w_{n,m}(z), \tag{2.17}$$

thereby coupling the fluid motion directly to the structural modes.

Using separation of variables, the general solution of (2.13), subject to the boundary conditions (2.14)–(2.15), can be expressed as

$$\phi(x, z) = \sum_{j=0}^{\infty} \left(B_j \, \mathrm{e}^{k_j x} + C_j \, \mathrm{e}^{-k_j x}\right) Z_j(z) \quad \text{for all } (x, z) \in \Omega, \tag{2.18}$$

where B_j and C_j are undetermined coefficients, and k_j are the positive roots of the dispersion relation

$$\omega^2/g + k_j \tan(k_j H) = 0, \quad j \in \mathbb{N}^+ \cup \{0\}. \tag{2.19}$$

Here, $k_0 = -\mathrm{i}k$ corresponds to the progressive wave mode, whereas $k_j \in \mathbb{R}^+$ for $j > 0$ corresponds to the evanescent modes.

The associated vertical eigenfunctions are given by (Mei 1992)

$$Z_j(z) = \frac{1}{\sqrt{N_j}} \cos\left[k_j (H + z)\right], \tag{2.20}$$

https://doi.org/10.1017/jfm.2026.11809 Published online by Cambridge University Press

where

$$N_j = \frac{\sin(2k_j H)}{4k_j H} + \frac{1}{2} \tag{2.21}$$

is the normalisation constant, chosen such that the eigenfunctions satisfy

$$\int_{-H}^{0} Z_j(z)\, Z_\zeta(z)\, \mathrm{d}z = H\delta_{j,\zeta} \tag{2.22}$$

for all $j, \zeta \in \{0\} \cup \mathbb{N}^+$.

To account for the edge singularity in the vicinity of the plate tips, the Galerkin method is employed so as to incorporate both the vanishing potential jump and the square-root velocity behaviour near the plate edges (Porter & Evans 1995). An auxiliary function is introduced to represent the horizontal velocity in the gap above submerged plate n:

$$U_n(z) = \sum_{q=0}^{\infty} U_{n,q}\, u_{n,q}(z) \quad \text{for} \quad (x, z) \in \Gamma_n^G, \tag{2.23}$$

where $\Gamma_n^G = \{(x_n, z) \mid -d_n < z < 0\}$ denotes the gap region, and $U_{n,q}$ are unknown coefficients.

The auxiliary basis functions are chosen to satisfy the free-surface condition and the convergence requirement at the edge $(x_n, -d_n)$. Thus $u_{n,q}(z)$ is defined by

$$u_{n,q}(z) - \frac{\omega^2}{g}\int_{-d_n}^{0} u_{n,q}(t)\, \mathrm{d}t = \frac{2(-1)^q}{\pi\sqrt{d_n^2 - z^2}}\, T_{2q}\left(\frac{z}{d_n}\right), \tag{2.24}$$

where T_{2q} is the Chebyshev polynomial of the first kind of degree $2q$.

2.2. *Finite array of flexible plates*

2.2.1. *Wave motion*

We consider a finite-sized FPMM assembly comprising N periodically arranged unit cells, as schematically illustrated in figure 1. A monochromatic incident wave train propagates along the positive x-direction, inducing hydroelastic oscillations of the flexible plates. Within the framework of linearised potential flow theory, the total velocity potential $\phi(x, z)$ can be partitioned into the incident potential ϕ^I, the diffraction potential ϕ^D (associated with the fixed structures), and the radiation potentials $\phi^{R,n,m}$ resulting from the modal oscillations of the plates. Specifically, the decomposition is expressed as

$$\phi = \phi^I + \phi^D + \sum_{n=1}^{N}\sum_{m=1}^{\infty} \dot{\sigma}_{n,m}\phi^{R,n,m}, \tag{2.25}$$

where $\dot{\sigma}_{n,m} = -\mathrm{i}\omega\sigma_{n,m}$ represents the complex velocity amplitude of the nth flexible plate oscillating in its mth natural mode. The radiation potential $\phi^{R,n,m}$ corresponds to the wave field generated by the mth mode of the nth plate in otherwise calm water.

The incident potential for a regular wave of amplitude A and angular frequency ω is defined by

$$\phi^I = -\frac{\mathrm{i}gA}{\omega}\frac{\cosh[k(z+H)]}{\cosh(kH)}\, \mathrm{e}^{\mathrm{i}kx}, \tag{2.26}$$

https://doi.org/10.1017/jfm.2026.11809 Published online by Cambridge University Press

where the wavenumber k is the positive real root of the linear dispersion relation at water depth H:

$$\omega^2/g = k\tanh(kH). \tag{2.27}$$

The unknown potentials ϕ^D and $\phi^{R,n,m}$ are governed by the Laplace equation within the fluid domain, subject to the standard free-surface and seabed boundary conditions. The kinematic boundary conditions on the surfaces of the plates Γ_n^P for a given potential ϕ^χ ($\chi \in \{D, (R, n, m)\}$) are stipulated as

$$\partial_x \phi^\chi = \begin{cases} -\partial_x \phi^I, & \chi = D \\ \delta_{n,i}\, w_{n,m}(z), & \chi = (R, n, m) \end{cases} \quad \text{for} \quad (x, z) \in \Gamma_n^P, \tag{2.28}$$

where $\delta_{n,i}$ denotes the Kronecker delta, signifying that for the radiation problem, only the nth plate is in motion. To ensure the uniqueness of the solution, the Sommerfeld radiation condition is imposed at infinity, requiring the scattered waves to be purely outgoing:

$$\lim_{x\to\pm\infty} \left(\partial_x \phi^\chi \mp \mathrm{i}k\phi^\chi\right) = 0. \tag{2.29}$$

The boundary-value problem is solved using the matched eigenfunction expansion method. The fluid domain Ω is partitioned into $N+1$ subdomains: the semi-infinite upstream region Ω_1, the interior regions between adjacent plates Ω_n ($n = 2, \ldots, N$), and the semi-infinite downstream region Ω_{N+1}, as depicted in figure 1. By invoking the separation of variables and satisfying the radiation conditions (2.29), the general solution for the diffracted and radiated velocity potential in each region is expanded as follows:

$$\phi_1^\chi = \sum_{j=0}^{\infty} B_{1,j}^\chi\, \mathrm{e}^{k_j x}\, Z_j(z), \quad (x, z) \in \Omega_1, \tag{2.30a}$$

$$\phi_n^\chi = \sum_{j=0}^{\infty} \left(B_{n,j}^\chi\, \mathrm{e}^{k_j x} + C_{n,j}^\chi\, \mathrm{e}^{-k_j x}\right) Z_j(z), \quad (x, z) \in \Omega_n\ (n = 2, \ldots, N), \tag{2.30b}$$

$$\phi_{N+1}^\chi = \sum_{j=0}^{\infty} C_{N+1,j}^\chi\, \mathrm{e}^{-k_j x}\, Z_j(z), \quad (x, z) \in \Omega_{N+1}, \tag{2.30c}$$

where $Z_j(z)$ are the vertical eigenfunctions, and k_j are the corresponding eigenvalues. The coefficients $B_{n,j}^\chi$ and $C_{n,j}^\chi$ are to be determined by invoking the continuity of pressure and horizontal velocity across the fluid interfaces at $x = x_n$. By exploiting the orthogonality of the eigenfunctions, the matching conditions are transformed into a truncated system of linear algebraic equations. The detailed algebraic procedure is relegated to Appendix A.

2.2.2. *Structural motion*

The dynamic response of the finite FPMM is governed by the structural equations of motion. For each resonator, the modal displacement amplitudes $\sigma_{n,m}$ are coupled with the fluid field via the hydrodynamic pressure. According to the modal expansion technique, the generalised wave force acting on the nth plate in its ζth mode is expressed as

$$F_{n,\zeta} = -\mathrm{i}\omega\rho_w \int_{-H}^{-d_n} \Delta\phi_n(z)\, w_{n,\zeta}(z)\, \mathrm{d}z = F_{n,\zeta}^e - \mathrm{i}\omega \sum_{p=1}^{N} \sum_{L=1}^{\infty} f_{n,\zeta}^{s,o} \sigma_{s,o}, \tag{2.31}$$

https://doi.org/10.1017/jfm.2026.11809 Published online by Cambridge University Press

where $F^{e}_{n,\zeta}$ represents the wave excitation force due to the diffraction of waves by the fixed array,

$$F^{e}_{n,\zeta} = \mathrm{i}\omega\rho_w \int_{-H}^{-d_n} \left(\phi^D \Big|_{x=x_n^-} - \phi^D \Big|_{x=x_n^+} \right) w_{n,\zeta}(z)\,\mathrm{d}z, \tag{2.32}$$

and $f^{s,o}_{n,\zeta}$ signifies the generalised radiation force on mode ζ of plate n caused by the unit-velocity oscillation of mode o of plate s. The radiation force is conventionally decomposed into added mass $a^{s,o}_{n,\zeta}$ and radiation damping $c^{s,o}_{n,\zeta}$ coefficients:

$$f^{s,o}_{n,\zeta} = \mathrm{i}\omega a^{s,o}_{n,\zeta} - c^{s,o}_{n,\zeta}. \tag{2.33}$$

By truncating the modal expansion at a sufficiently large order M, the coupled hydroelastic system can be cast into a compact matrix form,

$$\left[-\omega^2(\boldsymbol{M}_s + \boldsymbol{a}) - \mathrm{i}\omega\boldsymbol{c} + \boldsymbol{K} \right]\boldsymbol{X} = \boldsymbol{F_e}, \tag{2.34}$$

where $\boldsymbol{X}$ and $\boldsymbol{F}_e$ are the vectors of modal responses and excitation forces, respectively. The matrices $\boldsymbol{M}_s$ and $\boldsymbol{K}$ represent the intrinsic modal mass and stiffness of the plates, while $\boldsymbol{a}$ and $\boldsymbol{c}$ are the global added-mass and radiation damping matrices, capturing the hydrodynamic coupling between all resonators:

$$\boldsymbol{a} = [a^{s,o}_{n,m}]_{NM\times NM}, \quad \boldsymbol{c} = [c^{s,o}_{n,m}]_{NM\times NM}. \tag{2.35a,b}$$

The solution to (2.34) yields the structural response, from which the complete wave field is reconstructed via (2.25).

2.2.3. *Reflection and transmission coefficients*

The far-field performance of the FPMM array is characterised by the reflection (R) and transmission (T) coefficients. Based on the linearised free-surface condition, the wave elevation is given by $\eta = (\mathrm{i}\omega/g)\phi|_{z=0}$. In the asymptotic limit as $x \to \pm\infty$, only the propagating modes ($j = 0$) contribute to the wave elevation. Consequently, the coefficients are derived from the complex amplitudes of the reflected and transmitted waves:

$$R = \left| \frac{\mathrm{i}\omega\, Z_0(0)}{gA} \left(B^D_{1,0} + \sum_{n=1}^{N}\sum_{m=1}^{M} \dot{\sigma}_{n,m} B^{R,n,m}_{1,0} \right) \right|, \tag{2.36a}$$

$$T = \left| 1 + \frac{\mathrm{i}\omega\, Z_0(0)}{gA} \left(C^D_{N+1,0} + \sum_{n=1}^{N}\sum_{m=1}^{M} \dot{\sigma}_{n,m} C^{R,n,m}_{N+1,0} \right) \right|. \tag{2.36b}$$

For this non-dissipative potential flow problem, the energy conservation principle $R^2 + T^2 = 1$ is employed to verify the numerical consistency and convergence of the implemented method.

2.3. *Infinite array of flexible plates*

To elucidate the fundamental wave-steering properties and the emergence of bandgaps in the FPMM, we now extend the formulation to an infinitely periodic assembly of flexible plates along the x-axis. By invoking the discrete translational symmetry of the system, the analysis can be elegantly reduced to a single representative unit cell of length L. In accordance with the solution form established in § 2.2, the velocity potential in the fluid domains adjacent to the nth plate is represented as

https://doi.org/10.1017/jfm.2026.11809 Published online by Cambridge University Press

$$\phi_n = \sum_{j=0}^{\infty} \left(B_{n,j}\, \mathrm{e}^{k_j x} + C_{n,j}\, \mathrm{e}^{-k_j x} \right) Z_j(z), \quad (x, z) \in \Omega_n, \tag{2.37}$$

$$\phi_{n+1} = \sum_{j=0}^{\infty} \left(B_{n+1,j}\, \mathrm{e}^{k_j x} + C_{n+1,j}\, \mathrm{e}^{-k_j x} \right) Z_j(z), \quad (x, z) \in \Omega_{n+1}, \tag{2.38}$$

where $B_{n,j}$, $C_{n,j}$ and $B_{n+1,j}$, $C_{n+1,j}$ are the modal coefficients to be determined via the interfacial matching conditions.

Across the vertical interface at $x = x_n$, the continuity of the horizontal velocity and the pressure must be satisfied. The kinematic boundary condition, accounting for both the fluid gap and the hydroelastic motion of the plate, is given by

$$\partial_x \phi_n|_{x=x_n} = \partial_x \phi_{n+1}|_{x=x_n} = \begin{cases} U_n(z), & (x, z) \in \Gamma_n^G, \\ -\mathrm{i}\omega \sum_{m=1}^{\infty} \sigma_{n,m}\, w_{n,m}(z), & (x, z) \in \Gamma_n^P, \end{cases} \tag{2.39}$$

$$\phi_n|_{x=x_n} = \phi_{n+1}|_{x=x_n}, \quad (x, z) \in \Gamma_n^G. \tag{2.40}$$

To decouple the structural response from the fluid problem, the modal displacement $\sigma_{n,m}$ is expressed in terms of the potential jump $\Delta\phi_n$ by rearranging the dynamic equations (2.9) and (2.12):

$$\sigma_{n,m} = \frac{-\mathrm{i}\omega\rho_w \int_{-H}^{-d_n} \Delta\phi_n(z)\, w_{n,m}(z)\, \mathrm{d}z}{K_{n,m} - \omega^2 M_{n,m}}. \tag{2.41}$$

The spatial periodicity of the infinite lattice allows the application of Bloch's theorem (or Floquet theory). This theorem stipulates that the wave field in the $(n+1)$th cell is related to that in the nth cell via a complex phase modulation

$$\phi(x + L, z) = \mathrm{e}^{\mathrm{i}pL}\, \phi(x, z), \tag{2.42}$$

where p denotes the Bloch wavenumber. Due to the reciprocal nature of the lattice, the first Brillouin zone $p \in [0, \pi/L]$ is sufficient to characterise the dispersion properties. Consequently, the potential in the domain Ω_{n+1} can be mapped from the domain Ω_n as

$$\phi_{n+1} = \mathrm{e}^{\mathrm{i}pL} \sum_{j=0}^{\infty} \left(B_{n,j}\, \mathrm{e}^{k_j (x-L)} + C_{n,j}\, \mathrm{e}^{-k_j (x-L)} \right) Z_j(z), \quad (x, z) \in \Omega_{n+1}. \tag{2.43}$$

Substituting the periodic representations (2.37) and (2.43) into the continuity requirements (2.39) and (2.40), and projecting the resulting equations onto the orthogonal basis $Z_j(z)$, we obtain a system of governing equations for the unit cell. This formulation leads to a global homogeneous system of the form

$$\boldsymbol{S}(\omega, p)\, \boldsymbol{x} = \boldsymbol{0}, \tag{2.44}$$

where $\boldsymbol{x}$ is the vector of unknown coefficients defined as

$$\boldsymbol{x} = \left[B_{n,0}, \ldots, B_{n,J}, C_{n,0}, \ldots, C_{n,J}, U_{n,0}, \ldots, U_{n,Q} \right]^{\mathrm{T}}. \tag{2.45}$$

The transcendental coefficient matrix $\boldsymbol{S}$ encapsulates the hydroelastic coupling and the Bloch periodicity:

$$\boldsymbol{S} = \begin{bmatrix} S^{v,l}_{1,B} + S^{v}_{4,B} - \alpha S^{v}_{3,B} & S^{v,l}_{1,C} + S^{v}_{4,C} - \alpha S^{v}_{3,C} & -S^{v}_{2} \\ \alpha\left(S^{v,r}_{1,B} - S^{v}_{3,B}\right) + S^{v}_{4,B} & \alpha\left(S^{v,r}_{1,C} - S^{v}_{3,C}\right) + S^{v}_{4,C} & -S^{v}_{2} \\ S^{p}_{1,B} - \alpha S^{p}_{2,B} & S^{p}_{1,C} - \alpha S^{p}_{2,C} & \boldsymbol{0} \end{bmatrix} \tag{2.46}$$

https://doi.org/10.1017/jfm.2026.11809 Published online by Cambridge University Press

Parameter	Description	Value
g	Acceleration due to gravity	9.8 m s^{-2}
H	Water depth	1 m
ρ_w	Density of water	1000 kg m^{-3}
ρ_n	Density of plate n	1500 kg m^{-3}
l_n	Length of plate n	0.5 m
b_n	Width of plate n	0.01 m
E_n	Young's modulus of plate n	0.5 GPa

Table 1. Geometric and material properties of the fluid domain and the flexible plate. Note that each plate in the array has the same parameter values. Unless otherwise specified, these parameters remain constant throughout § 3.

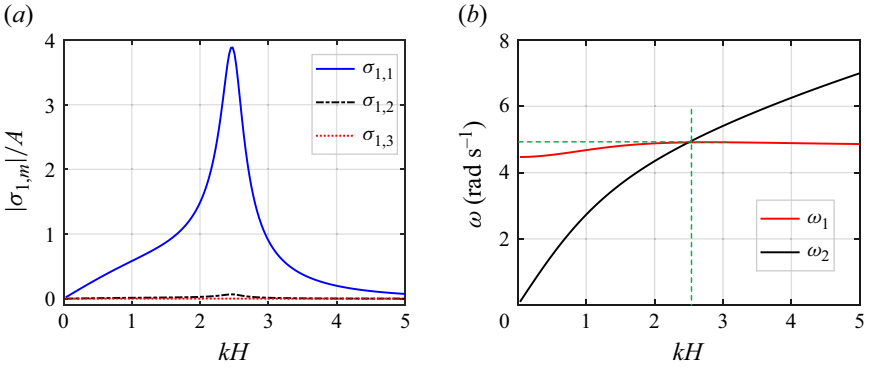


Figure 2. (*a*) Modal amplitude distributions of the first three elastic modes. (*b*) Graphical determination of the resonance frequency of the submerged flexible resonator.

where the constitutive sub-matrices are detailed in Appendix B.

The dispersion relation $\omega(p)$ is implicitly defined by the existence of non-trivial solutions to (2.44), requiring the vanishing of the determinant

$$\mathcal{D}(\omega,\, p) = \det[\boldsymbol{S}(\omega,\, p)] = 0. \tag{2.47}$$

For a prescribed real frequency ω, the roots p are generally complex. A purely real p corresponds to a propagating Bloch mode, signifying a passband, whereas a complex p with a non-zero imaginary part indicates spatial attenuation (evanescent modes), characterising the presence of a spectral bandgap.

3. Numerical results and discussion

3.1. *The LR mechanism*

In this subsection, we elucidate the fundamental dynamic characteristics of the FPMM by first examining the probative case of a solitary resonator interacting with monochromatic waves. The structural and fluid parameters prescribed for this canonical configuration are summarised in table 1.

The spectral response of the flexible plate, characterised by the amplitudes of the first three elastic modes, is depicted in figure 2(*a*). It is manifest that the first-order mode ($\sigma_{1,1}$) dominates the structural dynamics within the frequency range of interest, whereas higher-order modal contributions ($\sigma_{1,2}$, $\sigma_{1,3}$) remain negligible. This modal hierarchy not only

https://doi.org/10.1017/jfm.2026.11809 Published online by Cambridge University Press

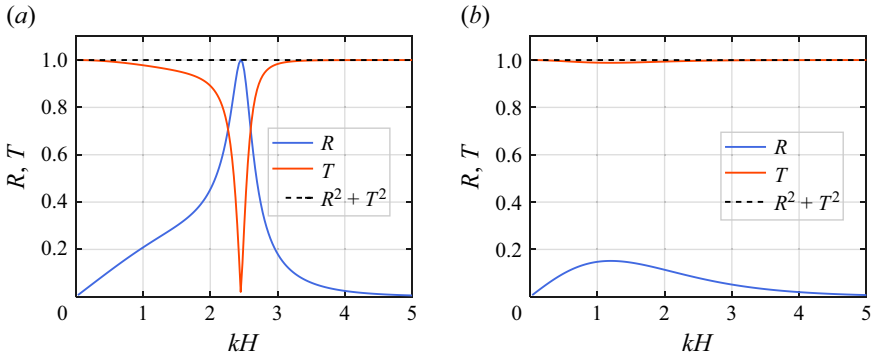


Figure 3. Coefficients of reflection (R) and transmission (T) for (a) a flexible resonator and (b) a fixed rigid plate as a function of the dimensionless wavenumber kH.

confirms the rapid convergence of our analytical solution, but also justifies the truncation at $M = 3$ for the subsequent parametric studies.

Determining the effective natural frequency of the resonator submerged in fluid necessitates accounting for the frequency-dependent hydrodynamic loading, specifically the added mass $a^{1,1}_{1,1}(\omega)$. Unlike a structure vibrating in a vacuum where the natural frequency remains static, the submerged flexible plate experiences frequency-dependent hydrodynamic added mass induced by the surrounding fluid. To identify the true resonant state of this coupled fluid–structure system, we employ a graphical approach as illustrated in figure 2(b). Here, the curve $\omega_1 = [K_{1,1}/(M_{1,1} + a^{1,1}_{1,1}(\omega))]^{1/2}$ represents the 'wet' natural frequency of the first-order structural mode (where the generalised modal mass $M_{1,1}$ and stiffness $K_{1,1}$ are defined via (2.11)), while the curve $\omega_2 = [gk\tanh(kH)]^{1/2}$ denotes the inherent dispersion relation of the water waves. Curves ω_1 and ω_2 create an intersection, where the ordinate corresponds to the resonator's natural frequency, and the abscissa represents the corresponding dimensionless wavenumber. The equilibrium point is found at $\omega = 4.85$ rad s^{-1} (corresponding to a dimensionless wavenumber $kH = 2.45$), which precisely aligns with the peak modal amplitude observed in figure 2(a).

The scattering performance of the resonator is quantified by the reflection (R) and transmission (T) coefficients, presented in figure 3(a). For comparison, the results for an equivalent rigid (fixed) plate are provided in figure 3(b). A salient feature of the flexible resonator is the emergence of a near-perfect reflection peak ($R \to 1$) at the resonance wavenumber $kH = 2.45$. In stark contrast, the rigid plate remains largely 'transparent' to the long-wave incident field, exhibiting minimal reflection. This marked disparity underscores that the wave attenuation is not merely a geometric scattering effect but is driven by the LR of the flexible structure. Furthermore, the identity $R^2 + T^2 = 1$ is strictly maintained across the spectrum, verifying the energy conservation and the numerical fidelity of our analytical solution.

To further visualise the LR effect, the spatial distributions of the normalised velocity potential amplitude $|\phi/\phi^I(0,0)|$ for both flexible and rigid cases are compared in figure 4. At the resonance frequency, the flexible plate induces a significant local energy amplification (near-field enhancement), as seen in figure 4(a). This energy entrapment is indicative of a strong coupling between the incident wave and the resonant mode, effectively creating a 'soft' boundary that thwarts wave transmission. Conversely, the potential field around the rigid plate (figure 4b) exhibits no such localisation, with the wave energy bypassing the structure unhindered. This contrast highlights that the flexible

https://doi.org/10.1017/jfm.2026.11809 Published online by Cambridge University Press

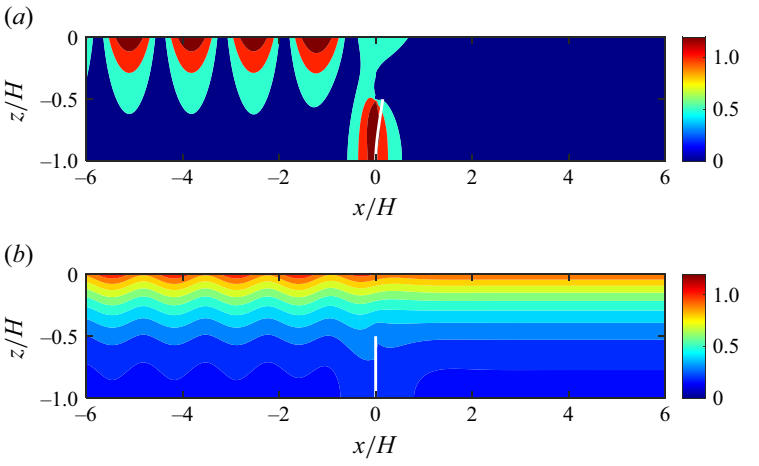


Figure 4. Normalised velocity potential fields at resonance ($\omega = 4.85$ rad s^{-1}, $kH = 2.45$). (*a*) Flexible resonator exhibiting local energy amplification. (*b*) Fixed rigid plate showing unimpeded propagation.

resonator acts as a localised energy sink/reflector, demonstrating its efficacy in wave attenuation.

The physical mechanism underlying this wave suppression is rooted in the destructive interference between different wave components. As per (2.25), the total field is a superposition of the incident wave η^I, the diffraction wave η^D from the stationary structure, and the radiation wave η^R induced by the plate's oscillation. We define the baseline scattered field as $\eta^S = \eta^I + \eta^D$. Figures 5(*a*) and 5(*b*) compare the amplitude and phase of η^S and η^R. It is observed that while η^S closely mirrors the incident wave, the radiation wave η^R attains a comparable amplitude but maintains an antagonistic phase relationship near resonance.

The amplitude and phase differences are explicitly plotted in figure 5(*c*). Crucially, at resonance, the radiation wave is exactly 180° out of phase with the baseline field ($\theta(\eta_R - \eta_S) = \pi$), leading to a complete phase cancellation in the transmission direction. This antiphase synchrony is a hallmark of LR-based metamaterials. The structural response in figure 5(*d*) further confirms that the resonator's motion is consistently in the quadrature-to-antiphase regime ($[\pi/2, \pi]$) relative to the excitation. Consequently, the energy is redirected upstream (reflection) rather than transmitted, as the group velocity vanishes in the vicinity of this resonant turning point.

It is worth noting that the observed wave inhibition is fundamentally a coherent wave-steering effect rather than a dissipative one. In the current potential flow framework, the energy conservation $R^2 + T^2 = 1$ is strictly maintained, confirming that the transmission minima arise from the phase cancellation between the incident and radiation fields rather than the bulk drag typically associated with flexible aquatic vegetation. This resonance-driven mechanism enables the system to achieve significant wave attenuation within a compact footprint, a regime where drag-based dissipation would be insufficient.

3.2. *Bandgap characteristics*

Building upon the single-resonator analysis, we now investigate the collective spectral properties of an FPMM array. We consider a finite assembly of $N = 8$ resonators, maintaining the constituent parameters consistent with table 1. Here, the lattice constant is set to $L = H$ to allow both the LR and BR bandgaps to manifest within a comparable

https://doi.org/10.1017/jfm.2026.11809 Published online by Cambridge University Press

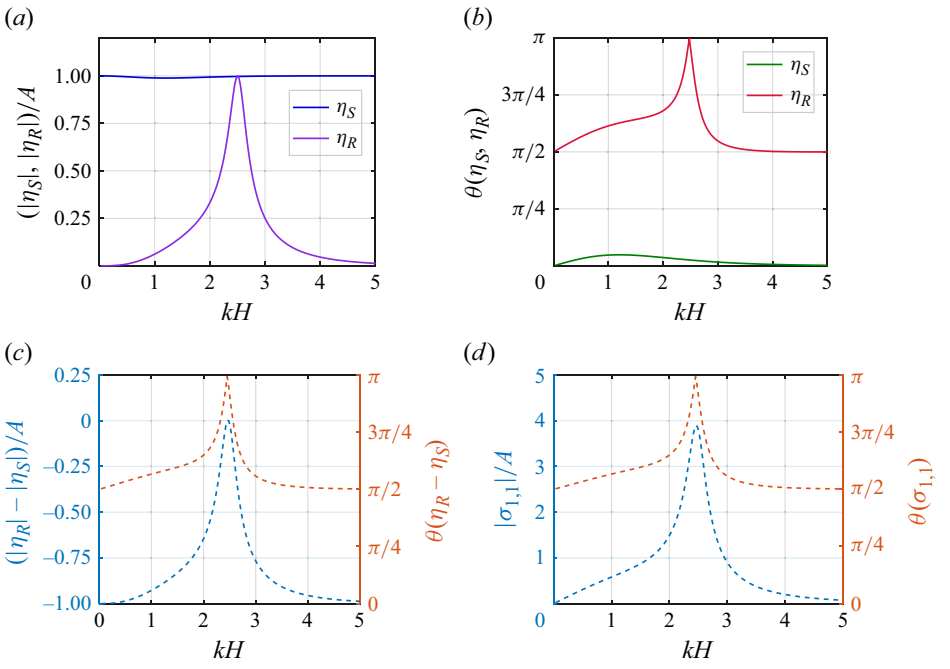


Figure 5. Mechanistic analysis of phase cancellation. (*a*) Amplitudes and (*b*) phases of the radiation (η^R) and baseline scattered (η^S) waves. (*c*) Amplitude difference and phase difference between η^R and η^S. (*d*) Modal response amplitude and phase of the flexible resonator.

frequency regime, which facilitates a clear and direct comparison of their underlying mechanisms and wave attenuation capabilities.

The scattering performance and dispersion topology of the FPMM are illustrated in figure 6. As shown in figure 6(*a*), a pronounced transmission minimum ($T \approx 0$) emerges within the interval $2.02 < kH < 2.45$. This region is in excellent agreement with the bandgap predicted by the infinite-array dispersion curves (figure 6*c*). The emergence of this bandgap is attributed to the coupling of the propagating water wave mode and the localised resonant mode of the flexible plates, leading to a zero-group-velocity regime (Ma & Sheng 2016). Significantly, the upper bound of this bandgap coincides with the intrinsic resonance frequency of an isolated resonator, confirming its classification as an LR bandgap. The transition from the single-plate response (figure 3*a*) to the array response (figure 6*a*) highlights the synergistic effect of periodic resonators, which respond collectively to the incident field to suppress wave transmission across a finite frequency band.

To distinguish the LR mechanism from conventional interference effects, the scattering coefficients for a rigid plate array are presented in figure 6(*b*). A distinct reflection peak is observed around $kH \approx 3$, governed by the BR condition. This occurs when the scattered waves from periodic heterogeneities interfere constructively, typically when the wavelength λ satisfies $2L/\lambda \approx 1$ (Mei 1985; Bragg & Bragg 1997). The inset in figure 6(*b*) confirms that the reflection maximum aligns with the Bragg criterion. For the FPMM array, figure 6(*c*) reveals a dual-bandgap structure: a low-frequency LR bandgap and a higher-frequency BR bandgap. Notably, the BR bandgap in the FPMM case (figure 6*c*) shift to higher frequencies compared to the rigid case (figure 6*d*). This deviation stems from the hydrodynamic radiation and mutual coupling between the oscillating plates,

https://doi.org/10.1017/jfm.2026.11809 Published online by Cambridge University Press

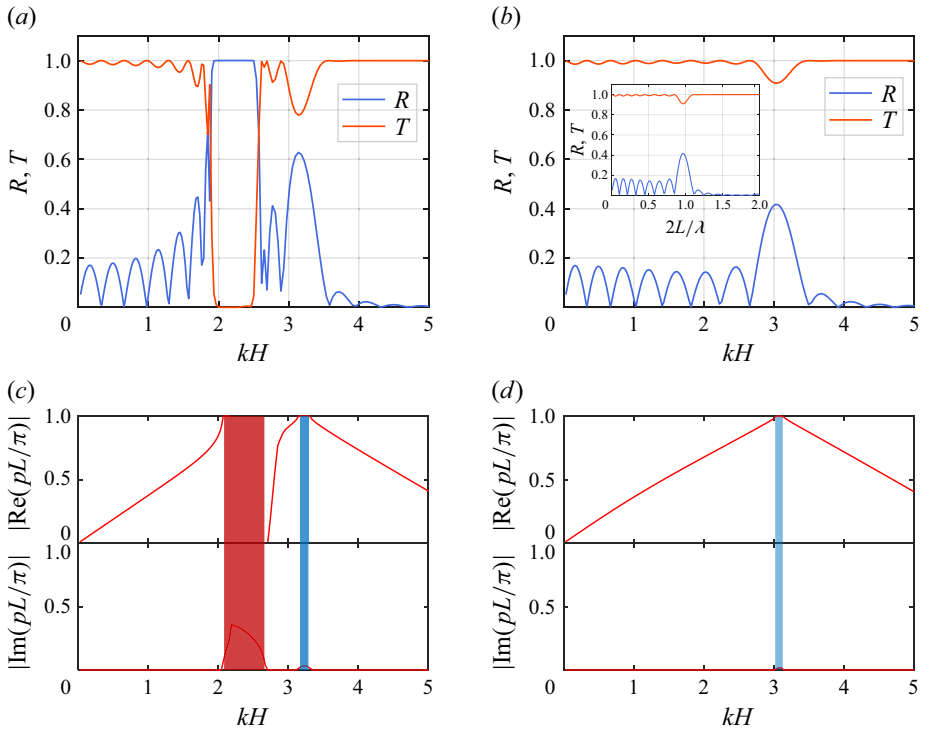


Figure 6. Wave scattering coefficients for $N = 8$ periodic cells: (a) flexible plates (FPMM) and (b) rigid plates. The inset in (b) depicts the coefficients versus the dimensionless wavelength $2L/\lambda$. Dispersion relations for infinite periodic arrays: (c) FPMM and (d) rigid plates.

which modify the effective periodicity of the system. Crucially, the LR bandgap is not only lower in frequency but also significantly broader than the BR bandgap, demonstrating the superior capacity of FPMMs for low-frequency wave control.

The spatial evolution of the wave field within the LR bandgap is further examined in figure 7. At a representative frequency ($kH = 2.1$), the instantaneous wave profiles (figure 7a) demonstrate that the radiation field η^R and the baseline scattered field η^S maintain a precise antiphase relationship. This destructive interference is the fundamental mechanism for the vanishing transmission observed in the array. Snapshots of the free-surface elevation and plate deformations at various time intervals (figure 7b) reveal a rapid spatial decay of the wave amplitude along the array. The upstream resonators intercept the majority of the wave energy, undergoing significant hydroelastic deformation, while the downstream resonators remain nearly quiescent. This effect is further corroborated by the velocity potential distribution in figure 7(c), where the localised energy concentration at the first resonator confirms that wave propagation is effectively halted before penetrating the bulk of the metamaterial.

Finally, we perform a parametric sensitivity analysis to assess the tunability of the LR bandgap. Figure 8(a) shows that increasing the elastic modulus E shifts the bandgap to higher frequencies, as the enhanced structural stiffness elevates the natural frequency of the resonators. Conversely, by reducing the modulus, the bandgap can be tuned towards the low-frequency regime. However, a common bottleneck in traditional acoustic metamaterials is that the bandgap bandwidth typically narrows as the central frequency decreases (Wang *et al.* 2014). As shown in figure 8(b), the FPMM exhibits a remarkable

https://doi.org/10.1017/jfm.2026.11809 Published online by Cambridge University Press

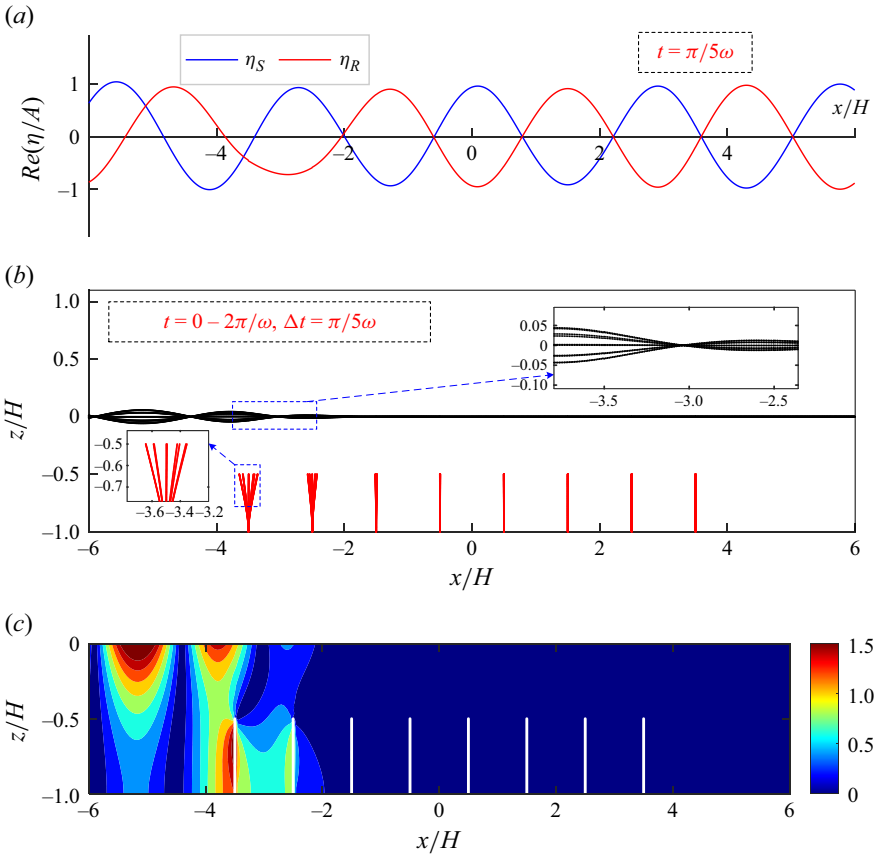


Figure 7. (*a*) Instantaneous wave profiles of the scattering and radiation components at $kH = 2.1$. (*b*) Temporal evolution of the wave elevation and plate response within one wave period. (*c*) Normalised velocity potential amplitude $|\phi/\phi^I(0, 0)|$, illustrating spatial attenuation.

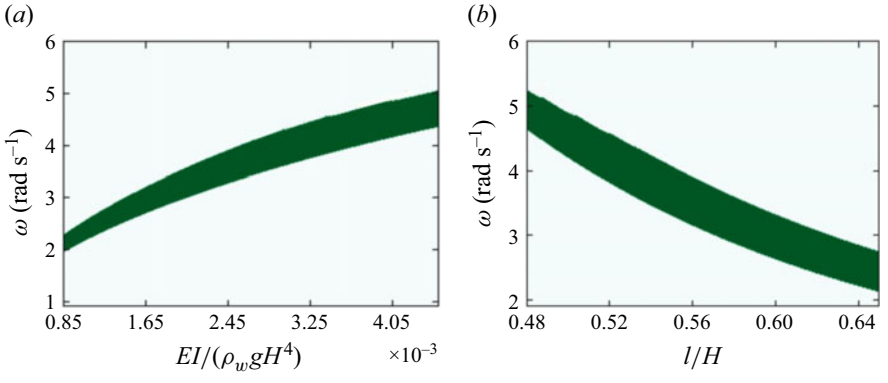


Figure 8. Evolution of the LR bandgap as a function of (*a*) the Young's modulus E, and (*b*) the plate length l. Other parameters are as specified in table 1.

https://doi.org/10.1017/jfm.2026.11809 Published online by Cambridge University Press

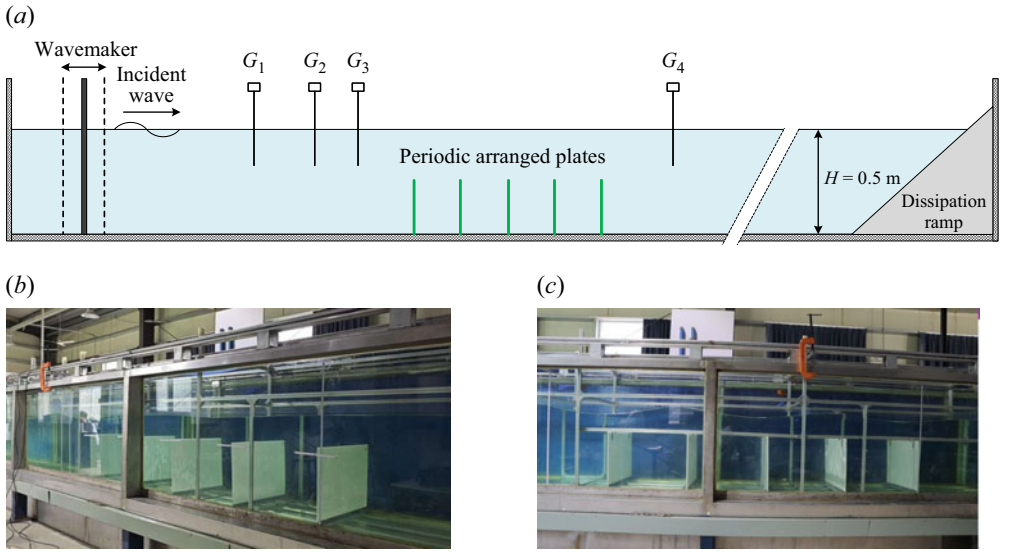


Figure 9. (*a*) Schematic of the experimental facility, instrumentation and physical model. Photographs show the experimental arrangement for (*b*) the flexible plate array and (*c*) the rigid plate array.

departure from this trend. While increasing the plate length l lowers the resonance frequency due to reduced stiffness, the bandgap width remains surprisingly robust. This phenomenon is rooted in the frequency-dependent nature of the fluid–structure interaction: as the plate size increases, the submerged surface area and the associated hydrodynamic added mass also increase. This compensatory mechanism sustains a strong hydroelastic coupling even at lower frequencies, allowing the FPMM to achieve a robust broadband attenuation performance.

4. Model experiments

The preceding theoretical analysis suggests that water wave bandgaps can be engineered using FPMMs. In this section, a series of laboratory experiments is presented to validate these theoretical predictions and assess the performance of the proposed device under physical conditions.

4.1. *Experimental set-up*

The experimental facility and the configuration of the physical model are illustrated in figure 9(*a*). The tests were conducted in a wave flume at the Port and Navigation Laboratory, Xiamen University of Technology, which measures 35 m in length, 0.7 m in width, and 0.8 m in depth. A piston-type wavemaker was employed at the upstream end to generate monochromatic waves, while a sloped porous beach was installed at the downstream end to minimise wave reflections. The free-surface elevation was recorded by four resistance-type wave gauges with sampling frequency 200 Hz. Three gauges (G_1, G_2 and G_3) were positioned upstream of the FPMMs to facilitate the separation of incident and reflected wave components, while a single gauge (G_4) was located downstream to measure the transmitted wave field.

The FPMMs investigated in this study consist of five periodic unit cells. As shown in figure 9(*b*), the plates were bottom-mounted with their transverse axes aligned parallel to the wave crests. The plates were fabricated from polypropylene, selected for its appropriate

https://doi.org/10.1017/jfm.2026.11809 Published online by Cambridge University Press

H (m)	A (m)	T_w (s)	l (m)	b (m)	ρ (kg m^{-3})	E (GPa)	L (m)
0.5	0.02	[0.7, 2.0]	0.35, 0.4	0.0048	912	1.74	0.5

Table 2. Experimental parameters for the water waves and the polypropylene plates. The structural properties represent the mean values obtained from material characterisation tests.

Configuration	cfg. 1	cfg. 2	cfg. 3	cfg. 4
Plate type	Rigid	Rigid	Flexible	Flexible
Length l (m)	0.35	0.4	0.35	0.40

Table 3. Summary of experimental test cases.

structural compliance. Two distinct plate lengths, $l = 0.35$ and 0.4 m, were tested, while the width was set to 0.696 m to ensure a small gap with the flume sidewalls, thereby allowing free deformation without frictional interference. Although the nominal thickness was 0.005 m, actual dimensions were subject to manufacturing tolerances. Consequently, the material properties – density ρ, thickness b, and Young's modulus E – were precisely measured for the specific polypropylene batch used. The averaged experimental parameters for both the fluid and the structure are summarised in table 2. Although polypropylene is viscoelastic, it is modelled as purely elastic with a constant Young's modulus. In our narrow, low-frequency test regime (0.5–1.4 Hz), the frequency dependence of the modulus is negligible. Additionally, the internal structural damping is orders of magnitude smaller than the highly dominant hydrodynamic damping, rendering viscoelastic effects secondary.

Each flexible plate was inserted into a U-shaped aluminium channel securely anchored to the flume bed (see figure 9*b*), ensuring a fully submerged condition. For comparative analysis, a rigid plate array was also tested. These rigid plates were also made of polypropylene, but with increased thickness of 0.01 m and significantly higher flexural rigidity. As depicted in figure 9(*c*), both the upper and lower edges of the rigid plates were firmly clamped to ensure that they remained immovable and non-deformable during wave action.

The lattice constant was set to $L = 0.5$ m to satisfy the Bragg condition within the target frequency range. The water depth H was maintained at 0.5 m, and the incident wave amplitude A was fixed at 0.02 m. To characterise the frequency response, each configuration was subjected to 21 regular wave conditions, with periods T_w ranging from 0.7 s to 2.0 s. This corresponds to angular frequency range $\omega \in [3.14, 8.98]$ rad s^{-1} and non-dimensional wavenumbers $kH \in [0.77, 4.11]$.

4.2. *Experimental results*

Systematic laboratory tests were performed on periodic arrays of both rigid and flexible plates to evaluate their wave attenuation performance and investigate the influence of plate length. The parameters for the four experimental configurations (cfgs 1–4) are summarised in table 3.

Figure 10 presents the dispersion curves, along with the transmission and reflection coefficients, as functions of the non-dimensional wavenumber kH for cfgs 1 and 3. As depicted in figure 10(*a*), the periodic rigid plates (cfg. 1) induce a BR bandgap

https://doi.org/10.1017/jfm.2026.11809 Published online by Cambridge University Press

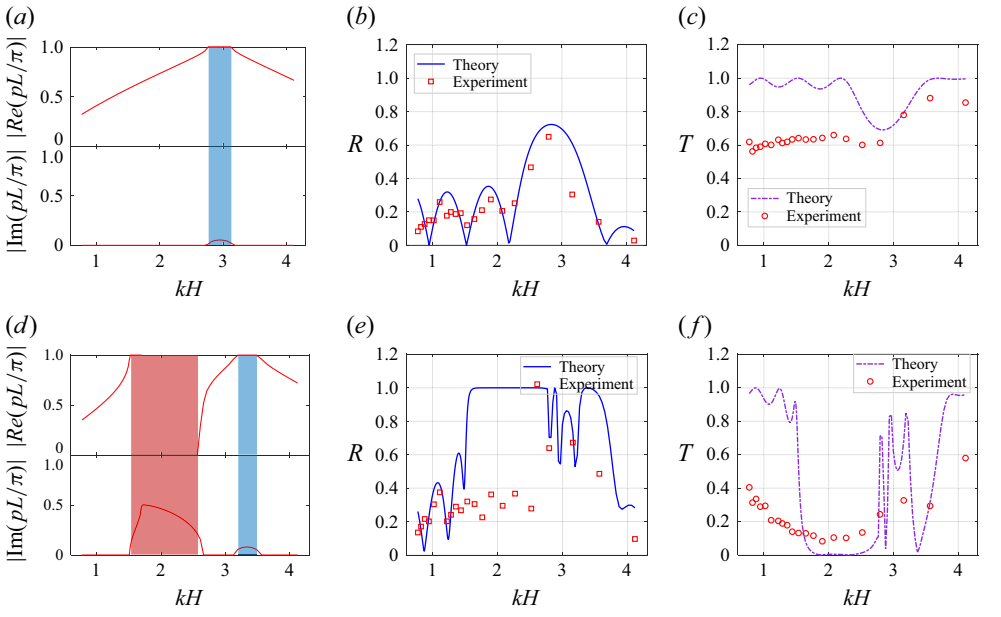


Figure 10. Dispersion curves for (*a*) periodic rigid plates and (*d*) periodic flexible plates ($l = 0.35$ m). Plots of the theoretical and experimental reflection and transmission coefficients for finite arrays (five cells) of (*b*,*c*) rigid and (*e*,*f*) flexible plates. Data for the rigid plate baseline are adapted from Jin *et al.* (2026) with permission.

within the range $kH \in [2.76, 3.12]$ under the prescribed geometry. For the finite array of rigid plates, the experimental reflection and transmission coefficients are compared with theoretical predictions in figures 10(*b*,*c*), respectively. A high degree of correlation is observed between the theoretical model and the experimental data in figure 10(*b*). The BR mechanism, characterised by enhanced reflection, is clearly identified and aligns well with the calculated bandgap. In figure 10(*c*), while the measured transmission coefficient follows the predicted trend, it remains consistently lower than the theoretical values. This discrepancy is attributed to viscous energy dissipation as waves propagate over the submerged obstacles (Cho *et al.* 2004), an effect neglected in the idealised potential flow model.

For the flexible plates (cfg. 3), the dispersion analysis in figure 10(*d*) predicts an LR bandgap at $kH \in [1.52, 2.59]$ and a subsequent BR gap at $kH \in [3.19, 3.48]$. The measured R and T for the finite flexible array are shown in figures 10(*e*) and 10(*f*). A prominent valley in the transmission coefficient is observed, with values approaching zero. The theoretical analysis confirms that this attenuation is driven by the LR mechanism. A secondary, shallower valley corresponding to the BR gap is also evident in the experimental data. However, notable deviations between the potential flow theory and experimental measurements occur within the LR band for the reflection coefficient (figure 10*e*). These discrepancies likely arise from nonlinear hydrodynamic effects, such as local wave breaking or vortex shedding at the plate tips, which will be further analysed in § 4.3.

The influence of increased plate length ($l = 0.4$ m) is illustrated in figure 11. For the rigid plates (cfg. 2), the BR bandgap shifts and widens to $kH \in [2.51, 3.12]$. Compared to cfg. 1 ($l = 0.35$ m), the increased length enhances wave reflection and further suppresses transmission, a trend consistently captured by both theory and experiment (figures 11*b*,*c*).

https://doi.org/10.1017/jfm.2026.11809 Published online by Cambridge University Press

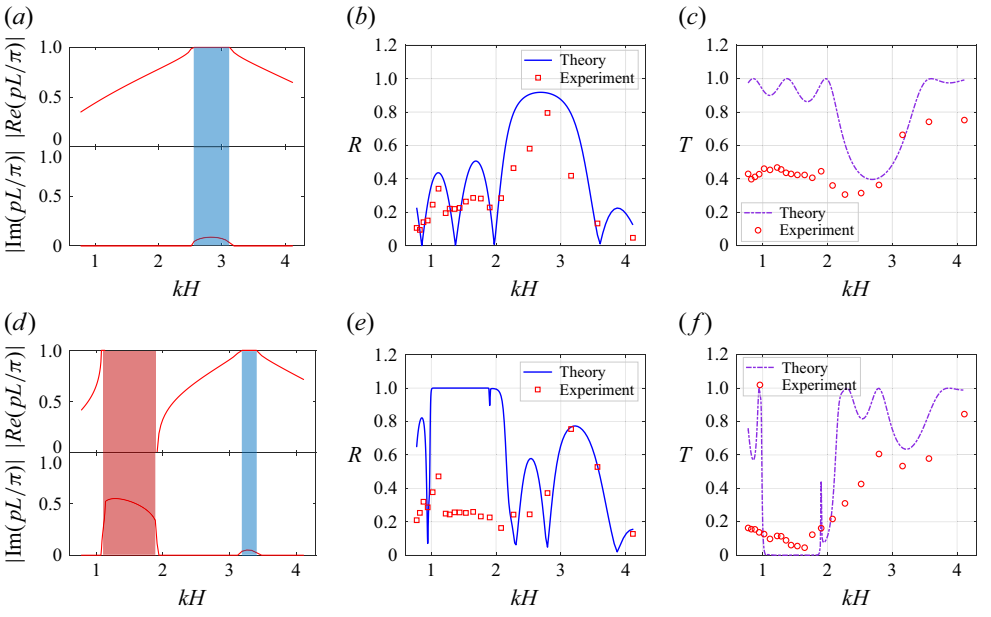


Figure 11. Experimental and theoretical results for plates with increased length ($l = 0.4$ m). The panels follow the same definitions as in figure 10.

The maxima in R and minima in T align precisely with the predicted bandgap region. For the periodic flexible plates (cfg. 4), LR and BR bandgaps coexist, as shown in figure 11(*a*). In comparison with the shorter plates ($l = 0.35$ m), the LR band shifts towards a lower-frequency regime (lower kH). This shift is physically consistent with the reduced effective stiffness of the longer plates. In figure 11(*e*), the theoretical reflection coefficient shows favourable agreement with experimental data, except in the resonance-dominated region $1.1 < kH < 2.0$. The transmission spectrum exhibits two distinct valleys corresponding to the LR and BR mechanisms. Notably, the experimental transmission coefficients within the LR band are significantly lower than those in the BR band. This confirms the superior wave attenuation capability of the LR mechanism, particularly for low-frequency broadband wave control.

4.3. *Energy dissipation*

The deviations observed between the theoretical predictions and experimental measurements can be attributed to several physical factors excluded from the linear, inviscid framework. These include flow separation at the sharp edges of the plates, viscous boundary layer effects, wave breaking, and nonlinear interactions between the incident, reflected and radiated wave components (De Vita *et al.* 2025). In this subsection, we quantify the experimental energy dissipation and analyse its underlying mechanisms.

To evaluate the energy loss, a dissipation coefficient is defined as

$$D = 1 - \left(R^2 + T^2\right). \tag{4.1}$$

In linear potential flow theory, D is identically zero. Thus any non-zero value of D serves as a metric for the energy extracted from the coherent wave field by dissipative or nonlinear processes.

Figures 12(*a*) and 12(*b*) illustrate the dissipation coefficients for rigid and flexible plates of different lengths. A significant amount of energy dissipation is evident in the

https://doi.org/10.1017/jfm.2026.11809 Published online by Cambridge University Press

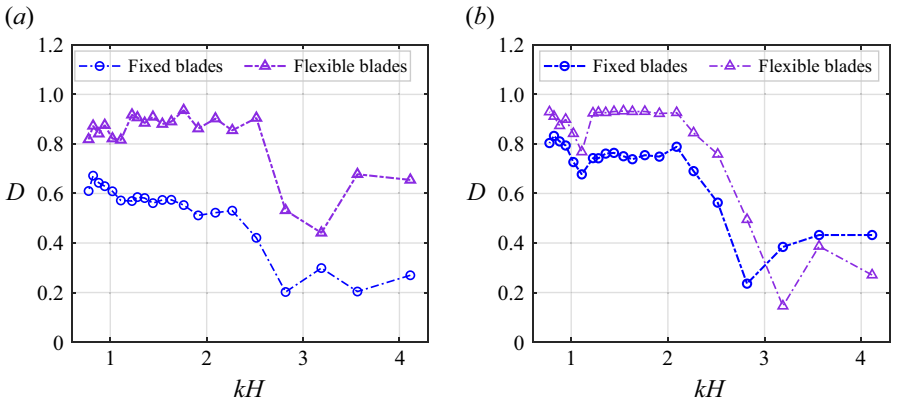


Figure 12. Energy dissipation coefficients D for incident waves interacting with rigid and flexible plate arrays, for plate lengths (*a*) $l = 0.35$ m, (*b*) $l = 0.4$ m.

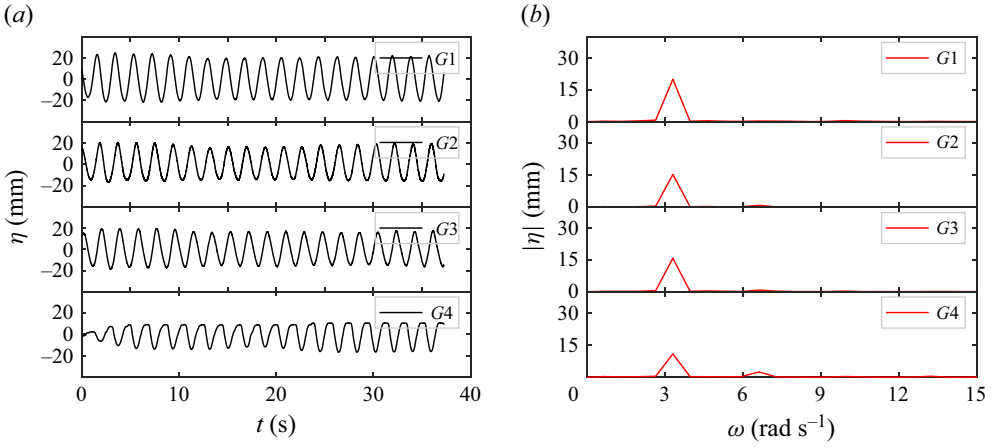


Figure 13. Experimental free-surface elevation and amplitude spectra for cfg. 1 at $T_w = 1.9$ s ($kH = 0.82$): (*a*) time series; (*b*) amplitude spectra derived via fast Fourier transform of five steady-state wave periods.

experimental data. For the shorter rigid plates ($l = 0.35$ m), $D \approx 0.5$ in the low-frequency regime ($kH < 2$), whereas for flexible plates, D reaches as high as 0.9. The increased dissipation in flexible plates suggests that the structural motion significantly enhances the conversion of wave energy into turbulence or higher-order harmonics. Notably, dissipation is more pronounced at low frequencies, which may be linked to larger particle excursion and higher horizontal velocities that promote flow separation. In figure 12(*b*), the overall trends remain consistent with the shorter plates, though the magnitude of D increases with plate length. Furthermore, D reaches a local minimum within the BR bandgap. This occurs because the majority of the incident energy is reflected by the periodic array, leaving only a small fraction to be dissipated via transmission through the structure.

One primary source of the apparent energy loss is the transfer of energy to higher-order harmonics via nonlinear interactions. Figure 13 presents the free-surface time series and corresponding frequency spectra for cfg. 1 at $T_w = 1.9$ s ($kH = 0.82$). As shown in figure 13(*a*), the transmitted amplitude at G_4 is substantially attenuated compared to the incident wave. While the upstream wave field (gauges G_1–G_3) remains nearly monochromatic, the downstream signal at G_4 exhibits distinct non-sinusoidal features. The

https://doi.org/10.1017/jfm.2026.11809 Published online by Cambridge University Press

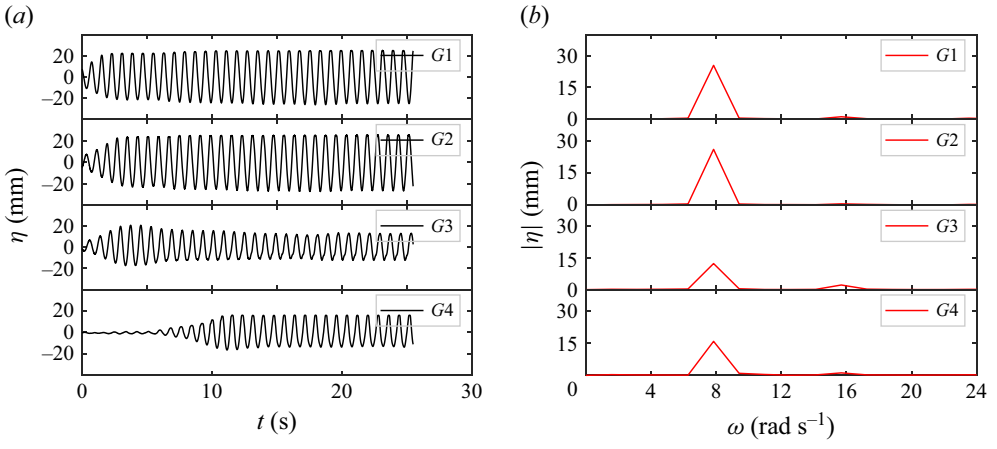


Figure 14. Experimental free-surface elevation and amplitude spectra for cfg. 1 at a shorter incident wave period $T_w = 0.8$ s ($\omega = 7.89$ rad s^{-1}, $kH = 3.19$): (*a*) time series; (*b*) wave amplitude spectra, where five wave periods (12–17 s) from the steady-state portion of the time series were used for fast Fourier transform analysis.

spectral analysis in figure 13(*b*) confirms that while the incident field is dominated by the fundamental frequency, the transmitted field contains measurable second-order harmonic components. This indicates a nonlinear energy cascade resulting from the interaction between the waves and the submerged obstacles. This process, as discussed by Li *et al.* (2021*a*,*b*) in the context of depth transitions, contributes to the observed discrepancy by redirecting energy from the primary wave frequency.

Flow separation at the plate edges also plays a critical role in energy dissipation. Comparison between the low-frequency results in figure 13 and the high-frequency results in figure 14 ($T_w = 0.8$ s, $kH = 3.19$) reveals that the high-frequency waveforms are significantly more stable. According to the dispersion relation, these shorter waves propagate with lower group velocities, which may reduce the intensity of vortex shedding. As noted by Polly *et al.* (2025), vortices generated at the edges of submerged elastic plates act as significant energy sinks, effectively draining energy from the primary wave mode.

The most prominent factor distinguishing flexible plates from rigid ones is the occurrence of localised wave breaking under resonance conditions. Figure 15 shows the sequential interaction between waves and flexible plates at $T_w = 1.2$ s ($kH = 1.54$). The lead plate undergoes high-amplitude pitch motion. As the plate moves from trough to crest (figures 15*a–d*), it acts as a secondary wave source, compressing the fluid and generating radiation waves. Near the equilibrium position (figure 15*c*), the plate velocity reaches its maximum, pushing the fluid with sufficient momentum to disrupt the circular orbital motion of the water particles, leading to localised breaking. This breaking process, coupled with the interference between incident and radiation waves, results in a standing-wave-like pattern characterised by severe energy dissipation. This explains why the experimental reflection coefficients for flexible plates are markedly lower than those predicted by potential flow theory.

The supplementary material includes two movies, are available at https://doi.org/10.1017/jfm.2026.11809 comparing the wave response for rigid (cfg. 1) and flexible (cfg. 3) arrays at $T_w = 1.0$ s ($kH = 2.09$, the resonant condition for the flexible array). Movie 1 demonstrates that while rigid plates provide some attenuation, significant wave energy still propagates downstream. In contrast, movie 2 shows that the flexible array effectively blocks the incident waves via the LR mechanism. The visible

https://doi.org/10.1017/jfm.2026.11809 Published online by Cambridge University Press

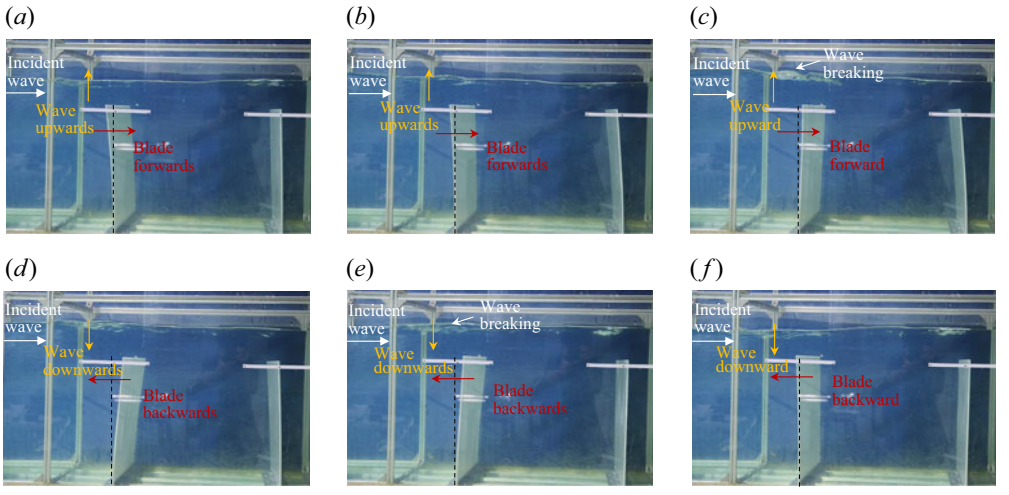


Figure 15. Photographs of wave interaction with resonant flexible plates ($l = 0.4$ m, $T_w = 1.2$ s, $kH = 1.54$). Panels (a)–(f) show the sequence at intervals $T_w/6$.

wave breaking in movie 2 further corroborates the role of nonlinear dissipation in the observed experimental results. In essence, the similar dissipation trends observed for rigid and flexible plates at low frequencies are fundamentally driven by incident wave kinematics. However, for the FPMMs, the LR mechanism acts as an amplifier. The localised energy trapping naturally forces the system into a highly dissipative nonlinear regime, significantly intensifying vortex shedding and wave breaking beyond what is achievable by rigid structures.

Although introducing a semi-empirical viscous drag term could force a closer agreement with experimental data, we retain the pure inviscid framework. The observed energy dissipation is driven by complex nonlinear phenomena – primarily localised wave breaking and vortex shedding – that a linearised drag coefficient cannot rigorously represent without *ad hoc* curve fitting. Preserving the baseline model thus avoids obscuring the underlying physics with empirical tuning.

In summary, the experimental findings confirm the superior wave attenuation capabilities of the LR mechanism in FPMMs. The empirical observation of Bragg reflection in rigid arrays and near-complete attenuation in resonant flexible arrays provides robust support for the proposed metamaterial-based wave control strategy.

5. Conclusion

In this study, the principles of metamaterial wave control are extended to the domain of water waves through the introduction of flexible plate metamaterials (FPMMs). A comprehensive theoretical framework, based on linear potential flow theory and the matched eigenfunction expansion method, has been developed to solve the underlying hydroelastic interaction problem. By integrating the modal expansion technique with Bloch's theorem, we have characterised the complex band structures of these periodic arrays, providing a rigorous evaluation of the wave attenuation performance and the associated hydrodynamic mechanisms.

The results elucidate the fundamental role of local resonance (LR) in suppressing surface gravity waves. We demonstrate that the interaction between incident waves and the elastic modes of the bottom-mounted plates leads to localised energy concentrations

https://doi.org/10.1017/jfm.2026.11809 Published online by Cambridge University Press

and the generation of significant backward-propagating radiation waves, which effectively neutralise the transmitted field. Notably, the LR-induced bandgaps are found to be substantially wider and situated at significantly lower frequencies compared to traditional BR bandgaps for a given lattice constant. This superior performance is attributed to the hydrodynamic added mass and the intrinsic flexibility of the plates, which facilitate sub-wavelength wave manipulation. The theoretical predictions were further corroborated by laboratory experiments in a wave flume, where the observed resonant attenuation showed agreement with the analytical dispersion relations.

While the present study establishes a solid conceptual paradigm, the complexity of real ocean environments introduces certain limitations. First, the linear, inviscid framework inherently neglects nonlinear wave interactions, vortex shedding and localised wave breaking – factors that contribute to the enhanced energy dissipation observed in our experiments. Second, the current two-dimensional approximation assumes normally incident waves. In realistic multi-directional sea states, obliquely incident waves could excite complex three-dimensional hydroelastic responses (such as torsional modes) and alter phase-matching conditions, which may compromise the array's overall wave-blocking efficiency. Extending this framework to capture fully three-dimensional, nonlinear and dissipative wave–structure interactions constitutes an essential direction for future investigations.

Beyond wave attenuation, the pronounced hydroelastic deformations of FPMMs under LR offer significant potential for multi-functional ocean engineering systems. Future studies will explore integrating power take-off systems – such as piezoelectric materials or electromagnetic generators – to enable simultaneous coastal protection and wave energy harvesting. Ultimately, this conceptual study demonstrates that leveraging structural hydroelasticity provides an efficient and tunable solution for low-frequency wave manipulation, mitigating coastal erosion, and protecting sensitive marine infrastructure.

Supplementary movies. Supplementary movies are available at https://doi.org/10.1017/jfm.2026.11809.

Funding. This research work has been funded by the National Natural Science Foundation of China (grant no. 12272128), the Natural Science Foundation of Jiangsu Province (grant no. BK20243019) and the Science, Technology Innovation Programme of Hunan Province (grant no. 2025RC3102).

Declaration of interests. The authors report no conflict of interest.

Data availability statement. The data that support the findings of this study are available from the corresponding author upon reasonable request.

Appendix A. Integral-equation method for the unknown wave potentials

An integral-equation technique is employed to determine the undetermined coefficients of the diffracted and radiated potentials. Following the formulation in § 2.2, the expressions for the wave potentials in respective fluid subdomains, as given by (2.16), are substituted into the continuity conditions (2.23) and (2.25) at the junctional interfaces. This yields

$$\sum_{j=0}^{\infty}\left(k_j B^{\chi}_{n,j}\,\mathrm{e}^{k_j x_n}-\delta^{*}_{n,1}k_j C^{\chi}_{n,j}\,\mathrm{e}^{-k_j x_n}\right)Z_j(z)=\sum_{j=0}^{\infty}\left(\delta^{*}_{n,N}k_j B^{\chi}_{n+1,j}\,\mathrm{e}^{k_j x_n}-k_j C^{\chi}_{n+1,j}\,\mathrm{e}^{-k_j x_n}\right)Z_j(z)$$
$$=\begin{cases}\sum_{q=0}^{\infty}U_{n,q}\,u_{n,q}(z), & x=x_n,\ z\in(-d_n,0]\\ \mu^{\chi}_{n}, & x=x_n,\ z\in[-H,-d_n)\end{cases}\tag{A1}$$

https://doi.org/10.1017/jfm.2026.11809 Published online by Cambridge University Press

and

$$\sum_{j=0}^{\infty}\left(B^{\chi}_{n,j}\,\mathrm{e}^{k_j x_n}+\delta^{*}_{n,1}C^{\chi}_{n,j}\,\mathrm{e}^{-k_j x_n}\right)Z_j(z)=\sum_{j=0}^{\infty}\left(\delta^{*}_{n,N}B^{\chi}_{n+1,j}\,\mathrm{e}^{k_j x_n}+C^{\chi}_{n+1,j}\,\mathrm{e}^{-k_j x_n}\right)Z_j(z), \tag{A2}$$

where $\delta^{*}_{n,i}=1-\delta_{n,i}$ denotes the modified Kronecker delta. To facilitate the solution, we define the integral identities

$$E_{n,q,j}=\int_{-d_n}^{0}u_{n,q}(z)\,Z_j(z)\,\mathrm{d}z=\frac{\cos(k_jH)\,J_{2q}(k_jd_n)}{\sqrt{N_j}}, \tag{A3}$$

where J_{2q} is the Bessel function of the first kind of order $2q$. Furthermore,

$$\begin{aligned}G_{n,m,j}&=\int_{-H}^{-d_n}w_{n,m}(z)\,Z_j(z)\,\mathrm{d}z\\&=\frac{1}{2\sqrt{N_j}}\left[\frac{\sin\left[(k_j+\kappa_{n,m})l_n\right]}{k_j+\kappa_{n,m}}+\frac{\sin\left[(k_j-\kappa_{n,m})l_n\right]}{k_j-\kappa_{n,m}}-\frac{\sin\left[(k_j+\mathrm{i}\kappa_{n,m})l_n\right]}{k_j+\mathrm{i}\kappa_{n,m}}\right.\\&\quad-\frac{\sin\left[(k_j-\mathrm{i}\kappa_{n,m})l_n\right]}{k_j-\mathrm{i}\kappa_{n,m}}+\xi_{n,m}\left(\frac{\cos\left[(k_j+\kappa_{n,m})l_n\right]-1}{k_j+\kappa_{n,m}}-\frac{\cos\left[(k_j-\kappa_{n,m})l_n\right]-1}{k_j-\kappa_{n,m}}\right.\\&\quad\left.\left.+\frac{\cos\left[(k_j+\mathrm{i}\kappa_{n,m})l_n\right]-1}{-\mathrm{i}k_j+\kappa_{n,m}}-\frac{\cos\left[(k_j-\mathrm{i}\kappa_{n,m})l_n\right]-1}{-\mathrm{i}k_j-\kappa_{n,m}}\right)\right]\end{aligned} \tag{A4}$$

and

$$\begin{aligned}P_{n,j,\zeta}&=\int_{-H}^{-d_n}\cos\left[k_j(z+H)\right]\cos\left[k_\zeta(z+H)\right]\mathrm{d}z\\&=\begin{cases}\dfrac{2k_\zeta l_n+\sin\left(2k_\zeta l_n\right)}{4k_\zeta}, & \zeta=j,\\[2ex]\dfrac{1}{2}\left(\dfrac{\sin\left[\left(k_j+k_\zeta\right)l_n\right]}{k_j+k_\zeta}+\dfrac{\sin\left[\left(k_j-k_\zeta\right)l_n\right]}{k_j-k_\zeta}\right), & \zeta\neq j.\end{cases}\end{aligned} \tag{A5}$$

By invoking the orthogonality of the eigenfunctions, we project the velocity identity (A1) onto $Z_\zeta(z)$ over the interval $z\in[-H,0]$, and the pressure identity (A2) onto $u_{n,\varsigma}(z)$ over $z\in[-d_n,0]$. This projection leads to

$$\begin{aligned}&\left(B^{\chi}_{n,\zeta}\,\mathrm{e}^{k_\zeta x_n}-\delta^{*}_{n,1}C^{\chi}_{n,\zeta}\,\mathrm{e}^{-k_\zeta x_n}\right)k_\zeta H=\left(\delta^{*}_{n,N}B^{\chi}_{n+1,\zeta}\,\mathrm{e}^{k_\zeta x_n}-C^{\chi}_{n+1,\zeta}\,\mathrm{e}^{-k_\zeta x_n}\right)k_\zeta H\\&=\sum_{q=0}^{\infty}U_{n,q}E_{n,q,\zeta}+\begin{cases}-\dfrac{gAk\,\mathrm{e}^{\mathrm{i}kx_n}}{\omega}\dfrac{P_{n,0,\zeta}}{\cosh(kH)\sqrt{N_\zeta}}, & \chi=D\\[2ex]\delta_{n,n}G_{n,m,\zeta}, & \chi=(R,n,m)\end{cases}\end{aligned} \tag{A6}$$

and

$$\sum_{j=0}^{\infty}\left(B^{\chi}_{n,j}\,\mathrm{e}^{k_j x_n}+\delta^{*}_{n,1}C^{\chi}_{n,j}\,\mathrm{e}^{-k_j x_n}\right)E_{n,\varsigma,j}=\sum_{j=0}^{\infty}\left(\delta^{*}_{n,N}B^{\chi}_{n+1,j}\,\mathrm{e}^{k_j x_n}+C^{\chi}_{n+1,j}\,\mathrm{e}^{-k_j x_n}\right)E_{n,\varsigma,j}. \tag{A7}$$

https://doi.org/10.1017/jfm.2026.11809 Published online by Cambridge University Press

The infinite series are truncated by retaining $J+1$ terms for the vertical eigenfunctions $Z_j(z)$, and $Q+1$ terms for the auxiliary functions $u_{n,q}(z)$. This truncation results in a closed complex linear system of order $(2J+Q+3)N$, which is solved numerically to determine the coefficients $B^{\chi}_{1,j}$, $B^{\chi}_{n,j}$, $C^{\chi}_{n,j}$, $C^{\chi}_{N+1,j}$, $U^{\chi}_{n,q}$.

Appendix B. Transfer matrix for the periodic cells

The transfer matrix characterising the periodic unit cells is derived by enforcing the continuity of pressure and velocity at the common interface. Substituting the expressions for the potential ϕ in subdomains Ω_n and Ω_{n+1} from (2.37) and (2.43) into the continuity conditions (2.39)–(2.40), and applying a Galerkin-type projection onto $Z_\zeta(z)$ and $U_{n,\varsigma}(z)$, we obtain

$$(B_{n,\zeta}-C_{n,\zeta})k_\zeta H=\sum_{q=0}^{\infty}U_{n,q}E_{n,q,\zeta}+\sum_{m=1}^{\infty}\tau_{n,m}G_{n,m,\zeta}\left(\mathrm{e}^{\mathrm{i}pL}\sum_{j=0}^{\infty}\left(B_{n,j}\,\mathrm{e}^{-k_jL}+C_{n,j}\,\mathrm{e}^{k_jL}\right)G_{n,m,j}-\sum_{j=0}^{\infty}(B_{n,j}+C_{n,j})G_{n,m,j}\right), \tag{B1}$$

$$\mathrm{e}^{\mathrm{i}pL}\left(B_{n,\zeta}\,\mathrm{e}^{-k_\zeta L}-C_{n,\zeta}\,\mathrm{e}^{k_\zeta L}\right)k_\zeta H=\sum_{q=0}^{\infty}U_{n,q}E_{n,q,\zeta}+\sum_{m=1}^{\infty}\tau_{n,m}G_{n,m,\zeta}\left(\mathrm{e}^{\mathrm{i}pL}\sum_{j=0}^{\infty}\left(B_{n,j}\,\mathrm{e}^{-k_jL}+C_{n,j}\,\mathrm{e}^{k_jL}\right)G_{n,m,j}-\sum_{j=0}^{\infty}(B_{n,j}+C_{n,j})G_{n,m,j}\right), \tag{B2}$$

$$\sum_{j=0}^{\infty}(B_{n,j}+C_{n,j})E_{n,\varsigma,j}=\mathrm{e}^{\mathrm{i}pL}\sum_{j=0}^{\infty}\left(B_{n,j}\,\mathrm{e}^{-k_jL}+C_{n,j}\,\mathrm{e}^{k_jL}\right)E_{n,\varsigma,j}, \tag{B3}$$

where $\tau_{n,m}=-\omega^2\rho/(K_{n,m}-\omega^2M_{n,m})$.

Upon truncating the vertical functions at $j=J$ and $q=Q$, respectively, (B1)–(B3) form a system with $2(J+Q)+3$ unknowns. Rearranging these terms yields the homogeneous matrix system

$$\begin{bmatrix} S^{v,l}_{1,B}+S^{v}_{4,B}-\alpha S^{v}_{3,B} & S^{v,l}_{1,C}+S^{v}_{4,C}-\alpha S^{v}_{3,C} & -S^{v}_{2} \\ \alpha\left(S^{v,r}_{1,B}-S^{v}_{3,B}\right)+S^{v}_{4,B} & \alpha\left(S^{v,r}_{1,C}-S^{v}_{3,C}\right)+S^{v}_{4,C} & -S^{v}_{2} \\ S^{p}_{1,B}-\alpha S^{p}_{2,B} & S^{p}_{1,C}-\alpha S^{p}_{2,C} & \mathbf{0} \end{bmatrix}\begin{bmatrix}\boldsymbol{B}_n\\ \boldsymbol{C}_n\\ \boldsymbol{U}_n\end{bmatrix}=\mathbf{0}, \tag{B4}$$

where $\alpha=\mathrm{e}^{\mathrm{i}pL}$ is the Bloch parameter, and $\boldsymbol{B}_n$, $\boldsymbol{C}_n$, $\boldsymbol{U}_n$ are column vectors of the unknown coefficients. The sub-matrices in (B4) are defined as

https://doi.org/10.1017/jfm.2026.11809 Published online by Cambridge University Press

$$\begin{cases} S^{v,l}_{1,B}(\zeta,\zeta) = -S^{v,l}_{1,C}(\zeta,\zeta) = k_\zeta H, \\ S^{v}_{2}(\zeta,q) = E_{n,q,\zeta}, \\ S^{v}_{3,B}(\zeta,j) = \mathrm{e}^{-k_j L}\,\tau^{\zeta,j}_{n,m}, \quad S^{v}_{3,C}(\zeta,j) = \mathrm{e}^{k_j L}\,\tau^{\zeta,j}_{n,m}, \\ S^{v}_{4,B}(\zeta,j) = \tau^{\zeta,j}_{n,m}, \quad S^{v}_{4,C}(\zeta,j) = \tau^{\zeta,j}_{n,m}, \\ S^{v,r}_{1,B}(\zeta,\zeta) = \mathrm{e}^{-k_\zeta L}\,k_\zeta H, \quad S^{v,r}_{1,C}(\zeta,\zeta) = -\mathrm{e}^{k_\zeta L}\,k_\zeta H, \\ S^{p}_{1,B}(\varsigma,j) = S^{p}_{1,C}(\varsigma,j) = E_{n,\varsigma,j}, \\ S^{p}_{2,B}(\varsigma,j) = \mathrm{e}^{-k_j L}\,E_{n,\varsigma,j}, \quad S^{p}_{2,C}(\varsigma,j) = \mathrm{e}^{k_j L}\,E_{n,\varsigma,j}. \end{cases} \tag{B5}$$

Here, $\tau^{\zeta,j}_{n,m} = \sum_{m=1}^{M} \tau_{n,m} G_{n,m,\zeta} G_{n,m,j}$, with indices ranging as $j, \zeta \in \{0, 1, \ldots, J\}$ and $q, \varsigma \in \{0, 1, \ldots, Q\}$.

References

Berraquero, C.P., Maurel, A., Petitjeans, P. & Pagneux, V. 2013 Experimental realization of a water-wave metamaterial shifter. *Phys. Rev. E* **88** (5), 051002.

Bragg, W.H. & Bragg, W.L. 1997 The reflection of X-rays by crystals. *Proc. R. Soc. Lond. Ser. A Contain. Pap. Math. Phys. Charact.* **88** (605), 428–438.

Cho, Y.-S., Lee, J.-I. & Kim, Y.-T. 2004 Experimental study of strong reflection of regular water waves over submerged breakwaters in tandem. *Ocean Engng* **31** (10), 1325–1335.

Dai, J., Wang, C.M., Utsunomiya, T. & Duan, W. 2018 Review of recent research and developments on floating breakwaters. *Ocean Engng* **158**, 132–151.

De Vita, F., De Lillo, F., Bosia, F. & Onorato, M. 2021 Attenuating surface gravity waves with mechanical metamaterials. *Phys. Fluids* **33** (4), 047113.

De Vita, F., de Tullio, M. D. & Onorato, M. 2025 On the local resonance between surface gravity waves and submerged resonators in a numerical wave tank. *J. Fluid Mech.* **1013**, A22.

Dupont, G., Remy, F., Kimmoun, O., Molin, B., Guenneau, S. & Enoch, S. 2017 Type of dike using C-shaped vertical cylinders. *Phys. Rev. B* **96** (18), 180302.

Falnes, J. 2002 *Ocean Waves and Oscillating Systems: Linear Interactions Including Wave-Energy Extraction*. Cambridge University Press.

Heathershaw, A.D. 1982 Seabed-wave resonance and sand bar growth. *Nature* **296** (5855), 343–345.

Hu, X. & Chan, C.T. 2005 Refraction of water waves by periodic cylinder arrays. *Phys. Rev. Lett.* **95** (15), 154501.

Hu, X., Chan, C.T., Ho, K.-M. & Zi, J. 2011 Negative effective gravity in water waves by periodic resonator arrays. *Phys. Rev. Lett.* **106** (17), 174501.

Huang, J. & Porter, R. 2023 Water wave propagation through arrays of closely spaced surface-piercing vertical barriers. *J. Fluid Mech.* **960**, A20.

Jin, H., Li, X., Ding, R., Xie, X., Zhou, J. & Zhang, H. 2026 Bragg scattering of surface gravity waves by periodic thin plates. *Thin-Walled Struct.* **222**, 114549.

Jin, H., Zhang, H., Lu, Y. & Xu, D. 2024 Floating periodic pontoons for broad bandgaps of water waves. *Appl. Math. Mech.* **45** (11), 1913–1928.

Jin, H., Zhang, H. & Xu, D. 2022 Array buoys with nonlinear stiffness enhance low-frequency wave attenuation and energy capture. *Phys. Fluids* **34** (12), 127106.

Lee, J. & Kim, Y.Y. 2023 Elastic metamaterials for guided waves: from fundamentals to applications. *Smart Mater. Struct.* **32** (12), 123001.

Li, Y., Draycott, S., Adcock, T.A.A., van den, B. & T. S. 2021*a* Surface wavepackets subject to an abrupt depth change. Part 2. Experimental analysis. *J. Fluid Mech.* **915**, A72.

Li, Y., Zheng, Y., Lin,, Adcock, T.A.A., van den, B. & T. S. 2021*b* Surface wavepackets subject to an abrupt depth change. Part 1. Second-order theory. *J. Fluid Mech.* **915**, A71.

Liang, H., Porter, R. & Zheng, S. 2024 Wave scattering by plate array metacylinders of arbitrary cross-section. *J. Fluid Mech.* **1001**, A6.

https://doi.org/10.1017/jfm.2026.11809 Published online by Cambridge University Press

LIU, H., FARHAT, M., BAGCI, H., GUENNEAU, S. & WU, Y. 2025 Broadband water wave reflector with customisable frequency range enabled by floating metaplates. *J. Fluid Mech.* **1020**, A50.
LIU, Y. & ZHANG, X. 2011 Metamaterials: a new frontier of science and technology. *Chem. Soc. Rev.* **40** (5), 2494.
LIU, Z., ZHANG, X., MAO, Y., ZHU, Y.Y., YANG, Z., CHAN, C.T. & SHENG, P. 2000 Locally resonant sonic materials. *Science* **289** (5485), 1734–1736.
LORENZO, M., PEZZUTTO, P., LILLO, F.D., VENTRELLA, F.M., VITA, F.D., BOSIA, F. & ONORATO, M. 2023 Attenuating surface gravity waves with an array of submerged resonators: an experimental study. *J. Fluid Mech.* **973**, A16.
MA, G. & SHENG, P. 2016 Acoustic metamaterials: from local resonances to broad horizons. *Sci. Adv.* **2** (2), e1501595.
MEI, C.C. 1985 Resonant reflection of surface water waves by periodic sandbars. *J. Fluid Mech.* **152**, 315–335.
MEI, C.C. 1992 *The Applied Dynamics of Ocean Surface Waves*. World Scientific.
MEI, C.C., STIASSNIE, M.A. & YUE, D.K.-P. 2018 *Theory and Applications of Ocean Surface Waves*, 3rd edn. World Scientific.
NOVÉ-JOSSERAND, C., GODOY-DIANA, R. & THIRIA, B. 2019 Interference model for an array of wave-energy-absorbing flexible structures. *Phys. Rev. Appl.* **11** (3), 034054.
POLLY, G., MÉRIGAUD, A., THIRIA, B. & GODOY-DIANA, R. 2025 Experiments on water-wave interactions with a horizontal submerged elastic plate. *J. Fluid Mech.* **1007**, R4.
PORTER, R. & EVANS, D.V. 1995 Complementary approximations to wave scattering by vertical barriers. *J. Fluid Mech.* **294**, 155–180.
PORTER, R., ZHENG, S. & LIANG, H. 2022 Scattering of surface waves by a vertical truncated structured cylinder. *Proc. R. Soc. A: Math. Phys. Engng Sci.* **478** (2258), 20210824.
SHENG, P., ZHANG, X.X., LIU, Z. & CHAN, C.T. 2003 Locally resonant sonic materials. *Phys. B: Condens. Matter* **338** (1), 201–205.
SIHVOLA, A. 2007 Metamaterials in electromagnetics. *Metamaterials* **1** (1), 2–11.
TORRES, M., ADRADOS, J.P. & MONTERO DE ESPINOSA, F.R. 1999 Visualization of Bloch waves and domain walls. *Nature* **398** (6723), 114–115.
WANG, P., CASADEI, F., SHAN, S., WEAVER, J.C. & BERTOLDI, K. 2014 Harnessing buckling to design tunable locally resonant acoustic metamaterials. *Phys. Rev. Lett.* **113**, 014301.
WESTCOTT, A.-R., BENNETTS, L.G., SERGIIENKO, N.Y. & CAZZOLATO, B.S. 2024 Broadband near-perfect capture of water wave energy by an array of heaving buoy wave energy converters. *J. Fluid Mech.* **998**, A5.
ZHELUDEV, N.I. & KIVSHAR, Y.S. 2012 From metamaterials to metadevices. *Nat. Mater.* **11** (11), 917–924.
ZHENG, S., LIANG, H. & GREAVES, D. 2024 Wave scattering and radiation by a surface-piercing vertical truncated metamaterial cylinder. *J. Fluid Mech.* **983**, A7.
ZHENG, S., PORTER, R. & GREAVES, D. 2020 Wave scattering by an array of metamaterial cylinders. *J. Fluid Mech.* **903**, A50.
ZHU, L., HUGUENARD, K., ZOU, Q.-P., FREDRIKSSON, D.W. & XIE, D. 2020 Aquaculture farms as nature-based coastal protection: random wave attenuation by suspended and submerged canopies. *Coast. Engng* **160**, 103737.
ZHU, S., ZHAO, X., HAN, L., ZI, J., HU, X. & CHEN, H. 2024 Controlling water waves with artificial structures. *Nat. Rev. Phys.* **6** (4), 231–245.
ZOU, S. *et al.* 2019 Broadband waveguide cloak for water waves. *Phys. Rev. Lett.* **123** (7), 074501.

https://doi.org/10.1017/jfm.2026.11809 Published online by Cambridge University Press